

The thesis committee for Heidi Seinige
certifies that this is the approved version of the following thesis:

**Magnetic Switching and Magnetodynamics
driven by Spin Transfer Torque**

**APPROVED BY
SUPERVISING COMMITTEE:**

Supervisor:

Maxim Tsoi

Alex de Lozanne

Magnetic Switching and Magnetodynamics
driven by Spin Transfer Torque

by

Heidi Seinige, B.S.

Thesis

Presented to the Faculty of the Graduate School

of the University of Texas at Austin

in Partial Fulfillment

of the Requirements

for the Degree of

Master of Arts

The University of Texas at Austin

December 2011

Acknowledgments

I would like to thank my supervisor Prof. Maxim Tsoi, for the great opportunity to work in his group. He gave me the chance, to gather many experiences and to develop new skills. Above all, I would like to thank him, for his patience and detailed explanations regarding any kind of problem.

I would also like to thank Fahmida Ferdousi and Urmimala Roy, for the great collaboration during the project about spin transfer torque driven magnetic switching. Within that, special thanks goes to Prof. Sanjay K. Banerjee, who made it possible for us to work together.

Special thanks go to my group member Cheng Wang and our "office-mate" Insun Jo for great discussions, conversations and also a lot of fun, in and outside of RLM. Next, I would like to thank Prof. Alex de Lozanne for serving as Co-Supervisor within my thesis.

Last but not least, I would like to thank my parents, my sister, and my friends, for always supporting me and believing in me.

Magnetic Switching and Magnetodynamics driven by Spin Transfer Torque

by

Heidi Seinige, M.A.

The University of Texas at Austin, 2011

Supervisor: Maxim Tsoi

In the scope of this thesis spin transfer torque (STT) driven switching and resonances in point contact experiments are investigated. In the first part, the focus is on STT driven switching events in magnetic devices with different tilt of the magnetization with respect to the thin film sample plane. Varying tilt is reached by different magnetic multilayers as Co/Ni and Co/Pt and the efficiency of STT is compared by measuring the magneto resistance (MR) traces. As expected it was observed that tilting the magnetization of one layer with respect to the other, can improve STT efficiency. This was confirmed by micromagnetic simulations using OOMMF.

In the second part of this thesis, STT driven resonances in an exchange-biased spin valve (EBSV) were investigated by applying ac (microwave) and dc currents while sweeping the applied magnetic field. The resulting magnetodynamics were observed by measuring the rectified voltage which appears

across the sample. To characterize the sample first the well known and understood ferromagnetic resonance (FMR) was excited. After that the power of the applied ac current was increased and a second resonance at a smaller magnetic field could be observed. This resonance structure was investigated and shown to be due to parametric resonance. This non-linear excitation appears in oscillator systems, if one or both parameter (damping, eigen frequency) oscillate in time. In the STT driven resonance experiments, the ac current causes the damping to oscillate and therefore drives the system into parametric resonance.

Contents

Acknowledgments	iii
Abstract	iv
List of Figures	viii
List of Tables	xii
Glossary	xiii
1 Introduction	1
2 Theory	3
2.1 Giant Magneto Resistance	3
2.2 Spin Transfer Torque	5
2.3 Spin Transfer Torque Driven Ferromagnetic Resonance	9
2.3.1 Conventional Ferromagnetic Resonance	9
2.3.2 Ferromagnetic Resonance with additional Spin Transfer Torque	16

2.4	Parametric Resonance	20
3	Experiment	26
3.1	Point Contact Technique	26
3.2	Spin Transfer Torque Driven Magnetic Switching	28
3.2.1	Micromagnetic Simulations	30
3.2.2	Sample Preparation and Characterization	31
3.2.3	Point Contact Experiments	38
3.2.4	Discussion	45
3.3	Spin Transfer Torque Driven Magnetodynamics	48
3.3.1	Set-up and Sample	48
3.3.2	Experiment - Ferromagnetic Resonance	50
3.3.3	Experiment - Parametric Resonance	54
3.3.4	Discussion	57
4	Summary and Outlook	58
	Bibliography	60

List of Figures

2.1	Schematic explanation of the GMR effect: The probability of an electron being scattered depends on the alignment of the electron's spin in respect to the magnetic field of the layer. The first layer acts as a spin polarizer, which filters the spin downs and allows spin ups to pass. The resistance of the whole structure depends consequently on the alignment of the two layers.	6
2.2	STT effect: For high external magnetic fields the magnetization of the two layers is almost aligned, for very low fields almost antiparallel. Electrons flowing from the left to the right side, get spin polarized by the first FM layer and because of Newton's third law exert a torque on the second FM layer in order to align both layers. Some electrons get reflected, bounce between the two layers, and exert higher order torques. But since the electron flux is lower after every reflection, the contribution is smaller the higher the order is.	8
2.3	a) Zeeman splitting the energy levels of a Spin 1/2 specimen in an external field \mathbf{B} . If the frequency of the rf field \mathbf{B}_{rf} matches the resonance conditions, the rf field is absorbed. b) precession of the magnetic moment in a static magnetic field \mathbf{B}_0 and the perpendicular applied rf field \mathbf{B}_{rf}	9
2.4	The influence of STT on the dynamics of the magnetization: In a) STT is parallel to the damping and therefore decrease it and the magnetization aligns quicker with the external field, whereas in b) the STT is antiparallel to the damping and therefore increases it.	17

2.5	Spin Transfer Diode Effect: The free layer magnetization of a SV oscillates in time due to the current induced torque. Since the resistance depends on the relative alignment of reference and free layer, it oscillates in time as well. The voltage is given by the product of current and resistance and the dotted line shows the average value, which appears as a rectified voltage across the SV.[12]	19
2.6	Simulation of conventional resonance: The x-axis represents time and the y-axis shows the amplitude. When the oscillator is excited by a driving force with frequency ω_0 , it starts to oscillate in time.	23
2.7	a and b show amplitude vs. time for parametric resonance in and outside of the instability zone. c shows a phase diagram of the parameters. The x-axis depicts the frequency, which excites the system and the y-axis the damping of the system. The black area represents a so called Arnold tongue, which is the area in parameter space, where parametric resonance is excited.	24
3.1	Simulation of magnetization dynamics at a current density of 4×10^{12} A/m ² a) $M_x(M_z)$ component of the free layer magnetization for in-plane (PMA and canted) SV: The switching time is improved for canted and perpendicular (PMA) magnetic anisotropy compared to the in-plane layer. b) Trajectory of the free layer magnetization during switching from parallel (P) to anti-parallel (AP) state for the canted spin valve. . . .	29
3.2	MFM scan of the demagnetized sample II. The scan area is $2\mu\text{m} \times 2\mu\text{m}$ and the black and white areas stand for domains with spin up and down. [49]	35
3.3	XRD analysis for sample II: Because of the very thin layers, only the peaks due to the thicker seed layers show up.	36
3.4	MR and EHE measurements for sample I to IV: All four samples show separate reference and free layer switching in the MR measurements, while in the EHE measurements, this can only be observed for sample I.	39
3.5	a) typical MR trace in point contact geometry for sample II b-d) Current vs. switching field for sample II, III and IV . . .	41

3.6	Grey scale plots for sample IV for up- and downsweep: The x-axis represents the applied magnetic field, the y-axis the applied dc current and different grey shades indicate different resistances (dark - low resistance; light - high resistance). The magnetic field was applied at different angles (0° , 45° and 90°) in respect to the plane of the sample. For 90° no distinct switching of the two layers can be observed. However for 0° and 45° distinct switching events are visible and for 45° STT effect can be observed.	44
3.7	3D plots of the angle dependence of sample V: The x-axis represents the applied field, the y-axis the angle of the applied in-plane field in respect to an arbitrary initial angle and different grey shades indicate different resistances (dark - low resistance; light - high resistance).	46
3.8	Schematic of the experimental set-up: A rf current, generated by a microwave generator, and a dc current are combined via a bias T and then injected through a point contact to the sample. An external magnetic field is applied by a pair of electric coils.	49
3.9	a) STT driven FMR at room temperature for a dc current of 21 GHz and no bias current applied to a 4.2Ω point contact b) linear dependence of the linewidth of the resonance signal on the applied dc current. Solid (open) circles refer to negative (positive) field.	51
3.10	a) Field dependence of the rectification signal measured at different frequencies of the applied dc current: with increasing frequency the resonance dips shifts to higher magnetic fields. b) Field dependence of STT driven FMR: closed circles show the measured dependence from a) and the solid line the expected FMR relationship for bulk NiFe.	52
3.11	a) Resonance structure for an applied dc current of 21GHz, a power of 12.3 dBm and a dc current of -11mA: The dip at about ± 280 mT corresponds to FMR, while the dip at about ± 90 mT can be assigned to parametric resonance. b) Trace of the rectified voltage for increasing power up to 14.8dBm: Starting at about 10.8 dBm the second resonance dip due to parametric resonance appears.	53

3.12	a) amplitude of FMR (closed circles) and parametric resonance (open circles) vs. the applied power b) Frequency vs. the switching field for FMR (closed circles) and parametric resonance (open circles) both fitted with equation 2.26.	55
3.13	Grey scale plots of the parametric excitation for different applied power values of the ac current: The x-axis represents the magnetic field, the y-axis the applied current, and the shade of the grey displays the measured rectified voltage (the darker the grey, the deeper the dip of the resonance structure) The dark areas represent Arnold tongues, which are an evidence for parametric excitations.	56

List of Tables

3.1	Switching current and switching time for different magnetization anisotropies obtained by micromagnetic simulations. . . .	28
3.2	Characteristic values for sample I to IV discussed in section 3.2.	33
3.3	XPS measurement for sample II [49]	34

Glossary

ac	Alternating current
AFM	antiferromagnetic
AFMR	Antiferromagnetic Resonance
AMR	Anisotropic Magneto Resistance
AP	Anti-Parallel
Ar	Argon
CIP	Current in Plane
Co	Cobalt
CPP	Current perependicular to Plane
Cu	Copper
dc	Direct current
EBSV	Exchange-biased Spin Valve
EHE	Extra-Ordinary Hall Effect
EPR/ESR	Electron Paramagnetic Resonance / Electron Spin Resonance
Fe	Iron
FM	ferromagnetic
FMR	Ferromagnetic Resonance
GMR	Giant Magneto Resistance
Ir	Iridium
KOH	Potassium Hydroxide
MgO	Magnesium Oxide

Mn	Manganese
MR	Magneto Resistance
MTJ	Magnetic Tunnel Junction
Ni	Nickel
NM	nonmagnetic
NMR	Nuclear Magnetic Resonance
P	Parallel
PMA	Perpendicular magnetic anisotropy
Pt	Platinum
RAM	Random Access Memory
rf	Radio Frequency
RMS	Root mean square
Si	Silicon
ST	Spin Transfer
STT	Spin Transfer Torque
SV	Spin Valve
VSM	Vibrating Sample Magnetometer
XPS	X-ray Photoelectron Spectroscopy
XRD	X-ray Diffraction

Chapter 1

Introduction

Conventional memory devices employ magnetic Oersted fields to induce magnetic switching [1]. However devices using the electron's spin, as a new degree of freedom, can be more efficient and therefore establish new opportunities in the field of electronics [2]. Spintronics, which is an acronym for spin transport electronics [3], includes the spin property of electrons in solid state devices, by either adding it to conventional charge based methods or using it exclusively [4]. Spin Transfer Torque (STT) memory devices can unify advantages of different technologies in one device and therefore become a new universal memory application. Magnetic switching induced by STT is more efficient and leads to lower switching currents and greater energy efficiency, while the memory device can still be nonvolatile [1].

This thesis is structured in two experiments, both focusing on spin dynamics altered by STT in magnetic multilayers. The first one investigates the influ-

ence of perpendicular magnetic anisotropy (PMA) and tilted magnetizations on switching times and currents, and the efficiency of STT. To compare the experiment with theoretical predictions, magnetodynamic simulations are done. Following this, experiments with samples of different tilt in the reference layer of the spin valve (SV) examine the efficiency of STT.

The second experiment uses resonances driven by STT to investigate the spin dynamics in an exchange-biased spin valve (EBSV). First the sample is characterized by conventional ferromagnetic resonance (FMR) and then the applied power is decreased to observe resonance driven by the oscillating damping parameter.

Chapter 2

Theory

2.1 Giant Magneto Resistance

The groundwork for nowadays spin-valve sensors in electric devices like STT-RAM, was laid by Albert Fert and co-workers [5], and Peter Grünberg [6] and co-workers in 1988 when they first observed giant magnetoresistance (GMR) in antiferromagnetically coupled FeCr multilayers. When the dimensions of a sample become comparable to the characteristic lengthscales of the magnetic and electric properties, such as the mean free path, new effects start to show up. This is due to quantum mechanical effects, which can couple the magnetic and electric properties of the sample.

If a structure, which shows GMR is brought into a magnetic field, one can see a drop in resistance assigned to GMR. This effect can be large compared to ordinary magnetoresistance (MR), which is due to the Lorentz force act-

ing on the electron's trajectory and anisotropic magnetoresistance (AMR), which arises from the higher probability of s-d-scattering of electrons moving in the direction of the magnetic field.

A simple, but straight forward model to describe GMR is Mott's two current model [7]. It assumes that the conductivity in a metal can be described by two independent channels, the spin up and spin down electron channel. This is justified, because the probability of spin-flip scattering in metals is very low compared to spin-conserving scattering events. The second assumption is, that the scattering rate in ferromagnetic (FM) materials is different for spin up and spin down electrons.

Of course this model is simplified and does not explain all details of the GMR effect, but it can easily illustrate the basic principle in magnetic multilayers. Figure GMR shows a spin valve (SV) consisting of two FM layers, FM1 and FM2, and a nonmagnetic (NM) spacer. The direction of the magnetization of the two separate layers depends on the external magnetic field. Different switching fields for FM1 and FM2 are achieved by various materials, different thicknesses of the layers or by pinning one of the layers by an additional antiferromagnetic (AFM) layer.

Assuming that the scattering is strong for electrons with spin antiparallel to the magnetization direction and weak for electrons with spin parallel, electrons with spin up can pass the first layer almost without any scattering process, while electrons with spin down are more likely to be scattered. Therefore the first layer acts like a spin filter for electrons with spin down.

If the second layer (FM2) is parallel to the first layer, electrons with spin up can easily pass through the device and a lower resistance is detected, than if the second layer is antiparallel in respect to the first one. MR is therefore defined as

$$\frac{\delta R}{R} = \frac{R_{ap} - R_p}{R_p} \quad (2.1)$$

with R_{ap} being the resistance in anitparallel state and R_p the resistance in parallel state. For current flowing in the plane of the thin layers (CIP), the effect disappears, if the thickness of the NM spacer exceeds the dimensions of the mean free path of the electrons. For current flowing perpendicular to the layers (CPP), the spin diffusion length is the critical factor. [8]

Apparently this is a simple picture of the GMR effect, not going into the microscopic details or considering any quantum mechanical effects, due to the small size of the device. To also include the effects of impurities, thickness of the layers, number of the layers, material, and temperature, more sophisticated models have to be developed. A summary is given in [9].

2.2 Spin Transfer Torque

The theory of spin transfer torque (STT) was developed by Berger and Slonczewski, who also suggested some of the new possibilities in electronic nano devices. The theory of STT is based on the fact, that an electrical

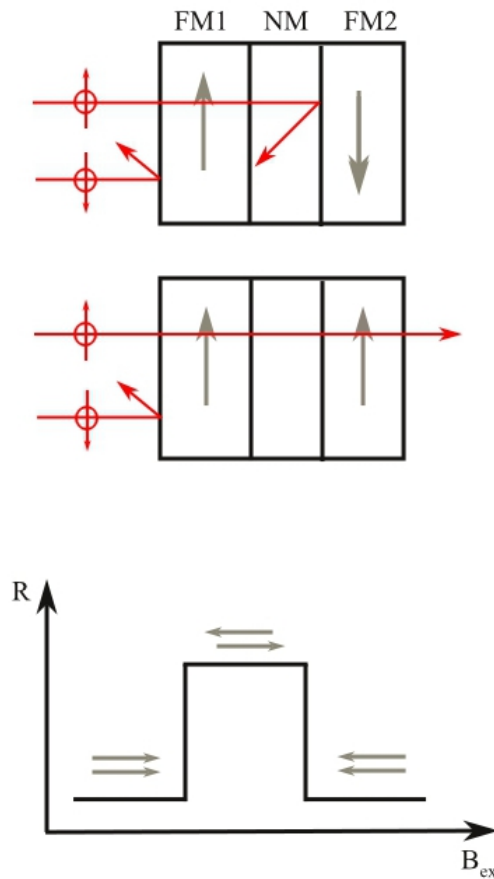


Figure 2.1: Schematic explanation of the GMR effect: The probability of an electron being scattered depends on the alignment of the electron's spin in respect to the magnetic field of the layer. The first layer acts as a spin polarizer, which filters the spin downs and allows spin ups to pass. The resistance of the whole structure depends consequently on the alignment of the two layers.

current does not only carry charge, but also angular momentum. In NM materials the orientation of the spins is statistically distributed, so there are no measurable effects on the device. In ferromagnetic materials, however, the spin current is partially polarized. This momentum can be absorbed by spin dependent scattering mechanisms and other processes in the lattice. To conserve momentum, the rate of change of momentum in the lattice due to these processes must be equal to the STT. It can excite magnons [10, 11, 8], switch the magnetization of nano devices [12, 13], and move domain walls [14]. Manipulating and exerting torque by STT in nano applications is more efficient than with Oersted fields, because it is scalable and therefore fulfills an essential property to be important in nanoscale electronics. [8]

To understand the idea of STT better, it is helpful to investigate the mechanisms in thin magnetic layers (figure2.2): If an electron is passing the interface of a NM layer to a FM layer and the magnetization is not aligned with the electron's spin, an reorienting exchange torque will act on the spin. And because of conservation of angular momentum, there needs to be a torque acting on the magnetization of the material.

Of course an observable influence on the magnetization of the magnetic layer is only reached with high current densities, since the transfer of angular momentum of a single electron is too small. This can be achieved by a mechanical point contact, which is described in section 3.1. To avoid that the distribution of individual electrons cancel each other, the current also needs to be spinpolarized, for example by an additional FM layer.

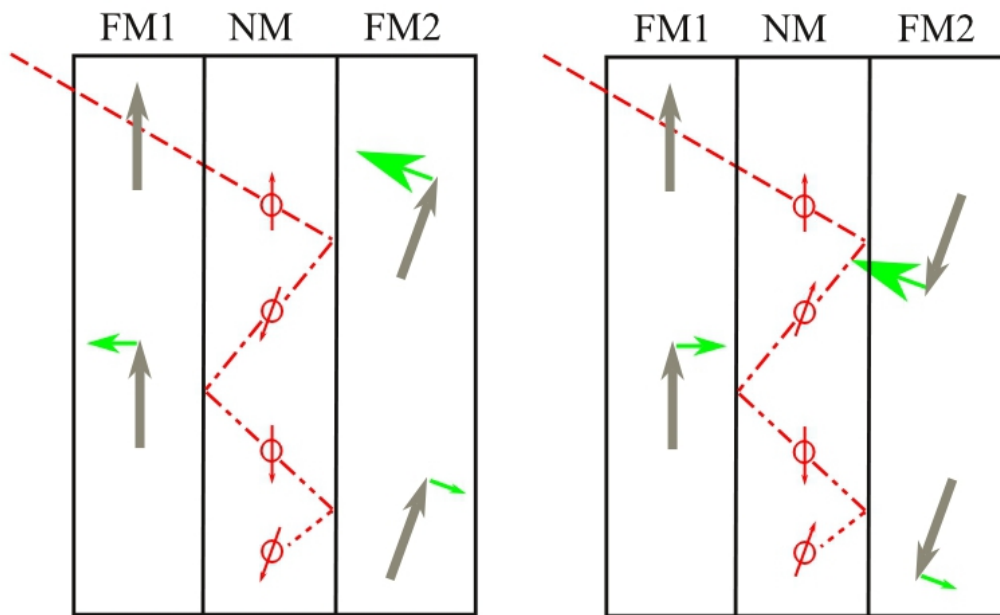


Figure 2.2: STT effect: For high external magnetic fields the magnetization of the two layers is almost aligned, for very low fields almost antiparallel. Electrons flowing from the left to the right side, get spin polarized by the first FM layer and because of Newton's third law exert a torque on the second FM layer in order to align both layers. Some electrons get reflected, bounce between the two layers, and exert higher order torques. But since the electron flux is lower after every reflection, the contribution is smaller the higher the order is.

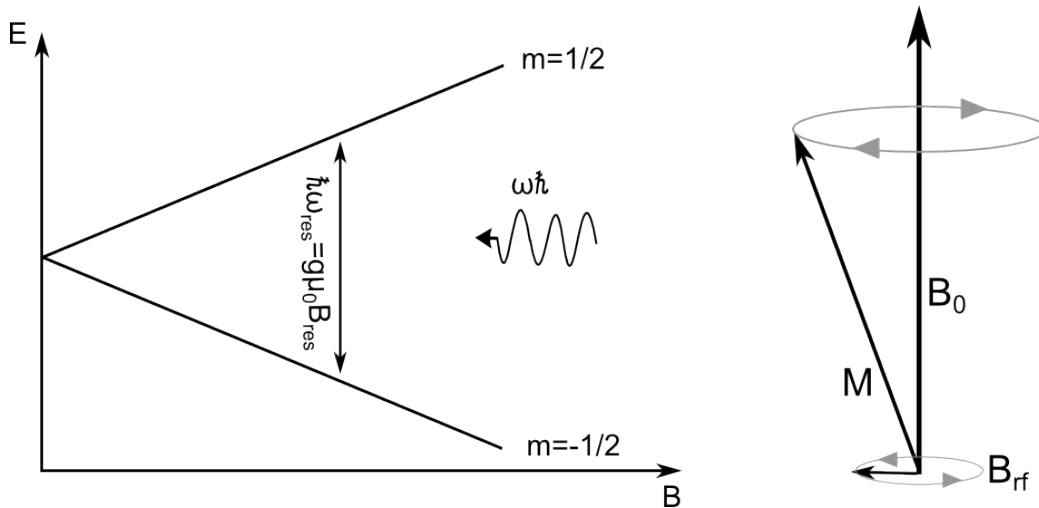


Figure 2.3: a) Zeeman splitting the energy levels of a Spin 1/2 specimen in an external field \mathbf{B} . If the frequency of the rf field \mathbf{B}_{rf} matches the resonance conditions, the rf field is absorbed. b) precession of the magnetic moment in a static magnetic field \mathbf{B}_0 and the perpendicular applied rf field \mathbf{B}_{rf}

2.3 Spin Transfer Torque Driven Ferromagnetic Resonance

2.3.1 Conventional Ferromagnetic Resonance

FMR is a widely used technique to probe magnetic characteristics of ferromagnetic materials. The physical principle of all magnetic resonance effects, such as EPR/ESR, AFMR or NMR are based on the precessional motion of magnetic moments in an external applied magnetic field. These effects give interesting insight into the structure of samples or are used in applications like magnetic resonance imaging [15].

Let us assume an arbitrary magnetic moment $\boldsymbol{\mu} = \gamma \boldsymbol{l}$ in a magnetic field \boldsymbol{B} , where γ is the gyromagnetic ratio and \boldsymbol{l} is the angular momentum vector. \boldsymbol{l} can be for example the spin of an electron, a nuclei or an atom. Due to the external magnetic field a torque

$$\boldsymbol{T} = \boldsymbol{\mu} \times \boldsymbol{B} \quad (2.2)$$

acts on the magnetic moment, which drives it into precession. The frequency of this precession is the so called Larmor frequency and is given by

$$f_L = \frac{\gamma B}{2\pi}. \quad (2.3)$$

This causes the Zeeman effect, which breaks the degeneracy of atomic states and is fundamental for magnetic resonance absorption. Obviously the field \boldsymbol{B} is a superposition of the external applied field \boldsymbol{B}_0 and the field created by the magnetic moments of the FM material. The interaction energy of the magnetic moment $\boldsymbol{\mu}$ and the magnetic field defining the absorption frequency is given by

$$U = -\boldsymbol{\mu} \cdot \boldsymbol{B}. \quad (2.4)$$

If we place the coordinate system so that \boldsymbol{B} is aligned with the z-axis the

energy of interaction transforms to

$$U = -\gamma\hbar Bl_z. \quad (2.5)$$

Thus the allowed energies of the system are

$$E = -\gamma\hbar Bm \quad m = l, l-1, \dots, -l \quad (2.6)$$

The energy difference between state i and k , which has to match the excitation energy $\hbar\omega$ is consequently

$$\delta E_{ik} = \gamma\hbar Bm_{ik}. \quad (2.7)$$

The absorption of external excitation is restricted by selection rules, which for the basic dipole approximation are

$$\delta m_{ik} = 0, \pm 1. \quad (2.8)$$

Since none of the Zeeman levels is degenerate, the only valid transition is $|\delta m_{ik}| = 1$. This can be excited by applying an additional alternating magnetic field \mathbf{B}_{rf} applied perpendicular to \mathbf{B} . Given these conditions we obtain

$$\omega_{res} = \gamma B \quad (2.9)$$

as a resonance condition for FMR. [16, 17]

We discussed that the presence of an external field can drive magnetic moments into precession. Now, we are going to investigate explicitly the dynamics, and finally introduce a phenomenological damping term.

The equation of motion for a magnetic moment in an external magnetic ($\mathbf{B}_0 = B_0 \mathbf{e}_x$) is [8]

$$\dot{\mathbf{M}} = \gamma \mathbf{M} \times \mathbf{B}_0. \quad (2.10)$$

The dynamics for x- and y-component are given by

$$\begin{pmatrix} \dot{M}_x \\ \dot{M}_y \end{pmatrix} = \gamma B_0 \begin{pmatrix} M_y \\ -M_x \end{pmatrix} \quad (2.11)$$

and by differentiating with respect to time we get

$$\begin{pmatrix} \ddot{M}_x \\ \ddot{M}_y \end{pmatrix} = \gamma B_0 \begin{pmatrix} \dot{M}_y \\ \dot{M}_x \end{pmatrix} = \gamma^2 B_0^2 \begin{pmatrix} -M_x \\ M_y \end{pmatrix} \quad (2.12)$$

Therefore the uncoupled equations of motion in time are

$$\begin{pmatrix} \ddot{M}_x \\ \ddot{M}_y \\ \ddot{M}_z \end{pmatrix} = \omega_0^2 \begin{pmatrix} M_x \\ M_y \\ 0 \end{pmatrix} \quad (2.13)$$

with $\omega_0^2 = \gamma^2 B_0^2$. The solution of these differential equations is the uniform

precession of the magnetic moment about \mathbf{B}_0 with an cone angle θ and total magnetic moment M_S [8]

$$M_x = M_S \sin \theta \exp(i\omega_0 t) \quad (2.14)$$

$$M_y = M_S \sin \theta \exp(i\omega_0 t + \pi/2) \quad (2.15)$$

$$M_z = M_S \cos \theta \quad (2.16)$$

However this precession cannot go on forever and eventually the magnetic moment will align with the external field. To describe this a phenomenological damping term has to be added to the equation of motion (equation 2.10). [8]

The physical reason for the damping lies in quantum-mechanical processes that perturb the precession. The mechanisms contributing to the damping can be for example spin-orbit, magnetostatic, electron-magnon, electron-phonon, and/or magnon-magnon interactions. Depending on the material and its intrinsic (presence of conducting electrons) and extrinsic (imperfections) factors the different mechanisms contribute to the perturbation. [1, 18]

There have been two approaches to account for the energy loss in the precession of a magnetic moment. One was introduced by Landau and Lifshitz

in 1935 [19]

$$\dot{\mathbf{M}} = \gamma' \mathbf{M} \times \mathbf{B}_0 - \gamma \frac{\lambda}{M} \mathbf{M} \times \mathbf{M} \times \mathbf{B}_0 \quad (2.17)$$

and one by Gilbert in 1956 [20]

$$\dot{\mathbf{M}} = \gamma \mathbf{M} \times \mathbf{B}_0 - \frac{\alpha}{M} \mathbf{M} \times \dot{\mathbf{M}}. \quad (2.18)$$

For $\alpha \ll 1$ and $\lambda = \alpha$ [8] or the substitutions [1]

$$\gamma' = \gamma / (1 + \alpha^2) \quad (2.19)$$

$$\lambda = \gamma \alpha / (1 + \alpha^2) \quad (2.20)$$

these two forms are equivalent. Both forms of the equation of motion have a spiralling solution that eventually aligns magnetic moment and field. The magnetization is rotated by both, the precession and damping, but does not change its length. [16] If $\alpha \gg 1$ the precession is overdamped and for $\alpha \ll 1$ the precession is only lightly damped and many precessions can take place before equilibrium is achieved.

Next we are going to discuss the resonance frequency and its dependency on the shape of the sample.[15] To derive this, we assume an elliptical shaped ferromagnetic insulator with a cubic lattice. The principal axes are the carte-

sian vectors $\mathbf{e}_x, \mathbf{e}_y$ and \mathbf{e}_z . N_x, N_y and N_z are the demagnetization factors, which are positive, depend on the ratio of the axes of the ellipsoid, and fulfill the condition $N_x + N_y + N_z = 1$.

The internal magnetic field \mathbf{B}_i of the specimen is subject to the external field \mathbf{B}_0 and the demagnetization factors

$$B_x^i = B_x^0 - N_x \mu_0 M_x; \quad B_y^i = B_y^0 - N_y \mu_0 M_y; \quad B_z^i = B_z^0 - N_z \mu_0 M_z \quad (2.21)$$

By neglecting the damping term in the Landau Lifshitz equation (equation 2.17 and 2.18), setting $dM_z/dt = 0$, $M_z = M$ (first order approximation), and $\mathbf{B}_0 = B_0 \mathbf{e}_z$, we get for the components of $\dot{\mathbf{M}}$

$$\frac{dM_x}{dt} = \gamma(M_y B_z^i - M_z B_y^i) = \gamma(B_0 + (N_y - N_z) \mu_0 M) M_y \quad (2.22)$$

$$\frac{dM_y}{dt} = \gamma(M(-N_x M_x) - M_x(B_0 - N_z M)) = -\gamma(B_0 + (N_x - N_z) \mu_0 M) M_x \quad (2.23)$$

Assuming an time-dependent $M \propto e^{-i\omega t}$ we get the eigen value problem:

$$\begin{vmatrix} i\omega & \gamma(B_0 + (N_y - N_z) \mu_0 M) \\ -\gamma(B_0 + (N_x - N_y) \mu_0 M) & -i\omega \end{vmatrix} = 0 \quad (2.24)$$

The solution of this eigen value problem is:

$$\omega_0^2 = \gamma^2(B_0 + (N_y - N_z)\mu_0 M)(B_0 + (N_x - N_z)\mu_0 M) \quad (2.25)$$

The resonance at frequency ω_0 is called the uniform mode, where all magnetic moments of the specimen precess in phase with same amplitude. In our FMR experiments we apply an external magnetic field parallel to the plane of the thin film sample, which leads to demagnetizations factors of $N_x = N_z = 0$ and $N_y = 1$. This gives the resonance frequency [15, 8]

$$\omega_0 = \gamma\sqrt{B_0(B_0 + \mu_0 M)} \quad (2.26)$$

2.3.2 Ferromagnetic Resonance with additional Spin Transfer Torque

To treat the dynamics of a spin including STT we can add a third term to the Landau Lifshitz Gilbert equation [21, 12]:

$$\dot{\mathbf{M}} = \gamma\mathbf{M} \times \mathbf{B}_0 - \frac{\alpha}{M}\mathbf{M} \times \dot{\mathbf{M}} + \eta\frac{I}{eMM'}\mathbf{M} \times (\mathbf{M}' \times \mathbf{M}) \quad (2.27)$$

where η is a factor describing the spin polarization and \mathbf{M}' is the polarization direction of the injected current. This additional term describes the torque acting on the magnetization due to ST and depends on the polarization rate η , the direction of the polarization and the current I . It can be parallel or

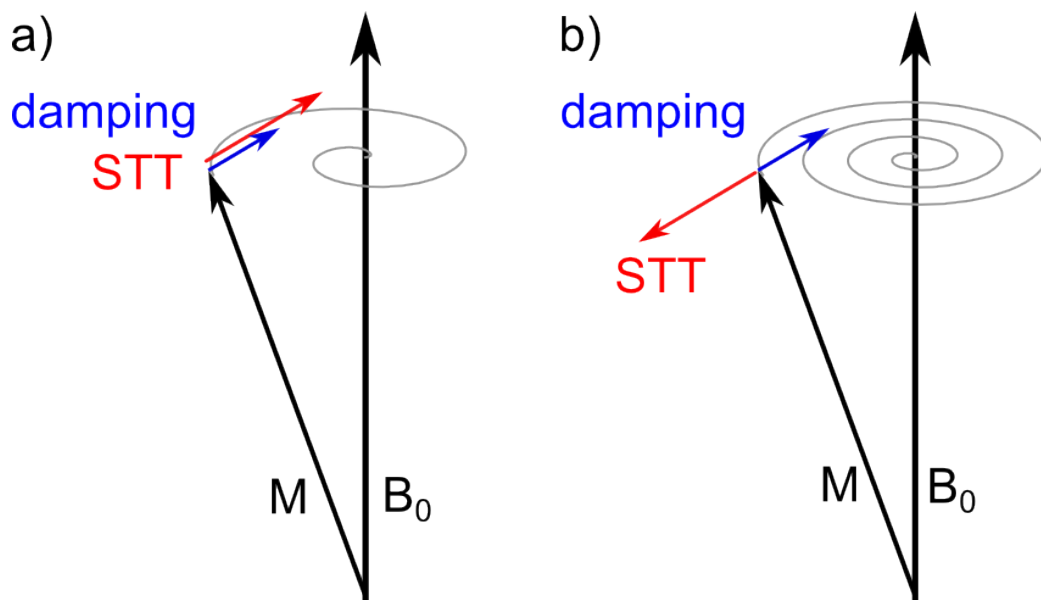


Figure 2.4: The influence of STT on the dynamics of the magnetization: In a) STT is parallel to the damping and therefore decrease it and the magnetization aligns quicker with the external field, whereas in b) the STT is antiparallel to the damping and therefore increases it.

antiparallel to the damping term, depending on the sign and therefore the direction of the current. As it can also be seen in figure 2.4, the torque due to ST can increase or decrease the damping, which can therefore be described by an effective damping

$$\alpha_{eff} = \alpha \left(1 - \frac{I}{I_c} \right). \quad (2.28)$$

The critical current I_c is the current for which the effective damping is zero and a stable precession is built up. It follows that FMR, which is usually driven by an external magnetic rf field \mathbf{B}_{rf} , can also be excited by STT using a rf current. This so called STT driven FMR has been theoretically predicted and experimental demonstrated in various paper [22, 23, 24, 25, 10, 26]. In the following the origin of the rectification signal, which is evidence of the FMR excited by STT is explained.

To detect STT driven FMR of a SV a rf current $I(t) = I_{rf} \cos(\omega t)$ is applied (see figure 2.5). This rf current exerts a torque on the free layer magnetization of the SV. If the frequency of the alternating current is close to the resonance frequency, the magnetic moment of the free layer starts to precess with the same frequency. Since the resistance of the SV depends on the relative alignment of the magnetization of free and reference layer, the resistance given by

$$R(t) = R_0 + R_1 \cos(\omega t - \delta) \quad (2.29)$$

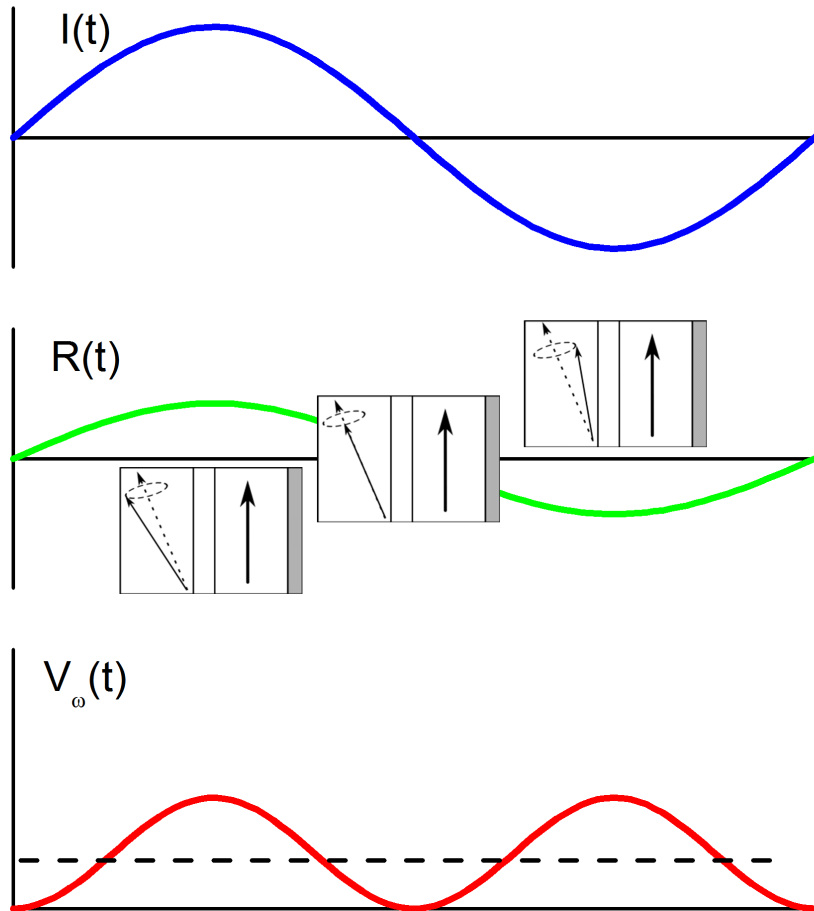


Figure 2.5: Spin Transfer Diode Effect: The free layer magnetization of a SV oscillates in time due to the current induced torque. Since the resistance depends on the relative alignment of reference and free layer, it oscillates in time as well. The voltage is given by the product of current and resistance and the dotted line shows the average value, which appears as a rectified voltage across the SV.[12]

will alternate in time as well. δ is the phase shift of the resistance with respect to the phase of the rf current. According to Ohms law, the voltage which can be measured is given by $I(t)V(t)$. $U(t)$ consists of time dependent terms with frequency ω and 2ω , and a time independent constant term, which is the time average voltage and is equal to [12]

$$V_\omega = \langle R_1 I_{rf} \cos(\omega t - \delta) \cos(\omega t) \rangle = 0.5 R_1 I_{rf} \cos \delta \quad (2.30)$$

This is an illustrative way to explain the rectified voltage measured in the experiments, a more mathematical way of the different distributions to the rectified voltage is given in [27].

2.4 Parametric Resonance

A child on a swing can excite motion by periodically changing its pose between standing and squatting. The variation of the height of the center of mass, changes the effective length of the swing. The change of the eigen frequency of the swing can then drive the system into resonance. The example of a child on a swing is a familiar representation of a parametric oscillator [28, 29, 30]. A parametric oscillator is defined by the fact, that one or both of its parameters (eigen frequency, damping) oscillate in time and therefore drive the system into resonance.

In the previous section we discussed that STT can change the damping of

spin precession in an external magnetic field and therefore defined an effective damping given by equation 2.28. If the applied current is a combination of ac and dc current, the effective damping will oscillate in time

$$\alpha(t) = \alpha_0 + \delta\alpha \cos(\omega t). \quad (2.31)$$

Consequently an ac current can drive the system in parametric resonance. The dynamics of this excitation and some simulations done by C. Wang with MATLAB are discussed following.

The dynamics of a magnetic moment in external field with damping are given by equation 2.18 and the demagnetization factors for a thin film in the xz-plane are given by $N_x=N_y=0$ and $N_z=1$ (section 2.3.1). The external magnetic field is applied along the z-direction $\mathbf{B} = B\mathbf{e}_z$. Thus we get with equations 2.21

$$\mathbf{M} = M_x\mathbf{e}_x + M_y\mathbf{e}_y + M_z\mathbf{e}_z \quad (2.32)$$

and

$$\mathbf{B} = B\mathbf{e}_z - \mu_0 m_y \mathbf{e}_y. \quad (2.33)$$

With the condition $\dot{M}_z = 0$ the components of equation 2.18 yield

$$\dot{M}_x = -\gamma(M_y B - M_z M_y) - \frac{\alpha}{M} \dot{M}_y M_z \quad (2.34)$$

$$\dot{M}_y = \gamma M_x B + \frac{\alpha}{M} M_z \dot{M}_x. \quad (2.35)$$

Differentiating equation 2.34 and 2.35, the x-component will yield

$$(1 + \alpha^2) \ddot{M}_x + [\gamma^2 B(B + \mu_0 M_z)] M_x + \alpha \frac{M_z}{M} \gamma (\mu_0 M_z + 2B) \dot{M}_x = 0. \quad (2.36)$$

With the eigen frequency $\omega_0 = \gamma^2 B(B + \mu_0 M_z)$ and the approximation

$$\begin{aligned} & \alpha \gamma \frac{M_z}{M} (\mu_0 M_z + 2B) \\ & \simeq 2\alpha \gamma B \left(\frac{\mu_0 M_z}{2B} + 1 \right) \\ & \simeq 2\alpha \gamma B \left(\frac{\mu_0 M_z}{B} + 1 \right)^{1/2} \\ & \simeq 2\alpha \omega_0 \end{aligned}$$

the x-component simplifies to

$$\ddot{M}_x + \omega_0^2 M_x + 2\alpha(t)\omega_0 \dot{M}_x = 0 \quad (2.37)$$

where the timedependent damping is given by equation 2.31.

With this equation, conventional resonance as well as parametric resonance can be simulated. For conventional resonance, the damping is set to be constant in time. Resonance can be observed, if a sinusoidal driving force with a frequency of ω_0 is added on the right side of equation 2.37. This

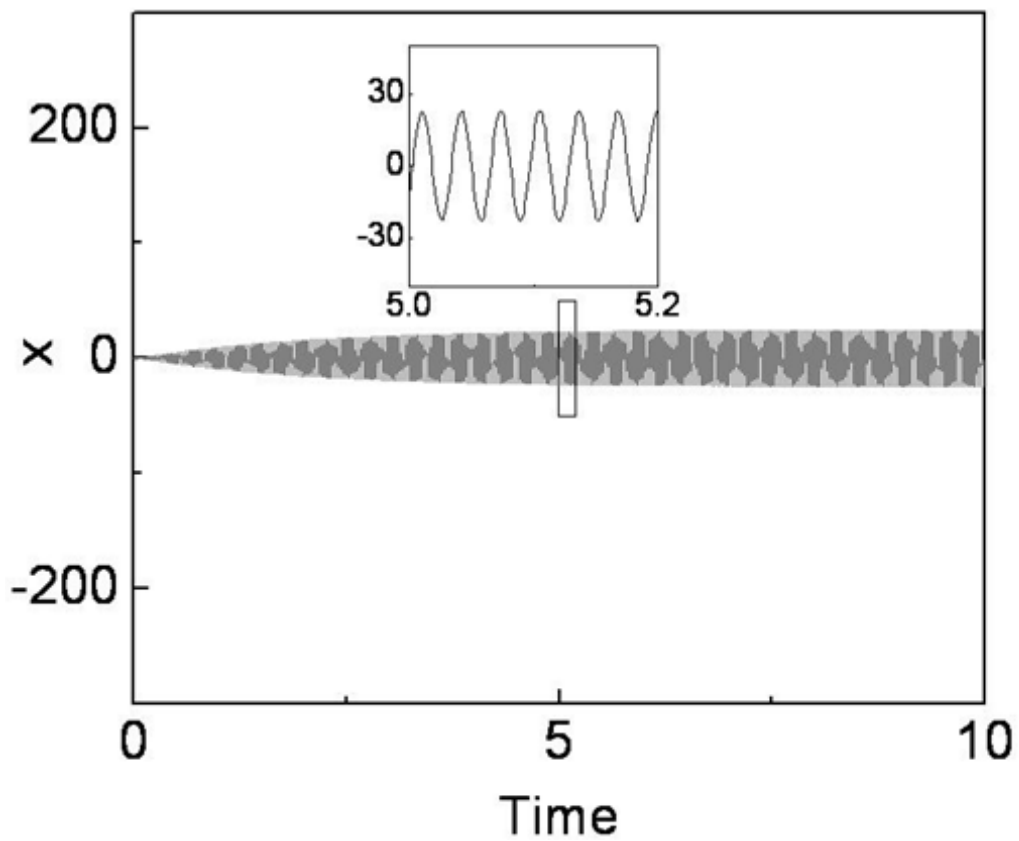


Figure 2.6: Simulation of conventional resonance: The x-axis represents time and the y-axis shows the amplitude. When the oscillator is excited by a driving force with frequency ω_0 , it starts to oscillate in time.

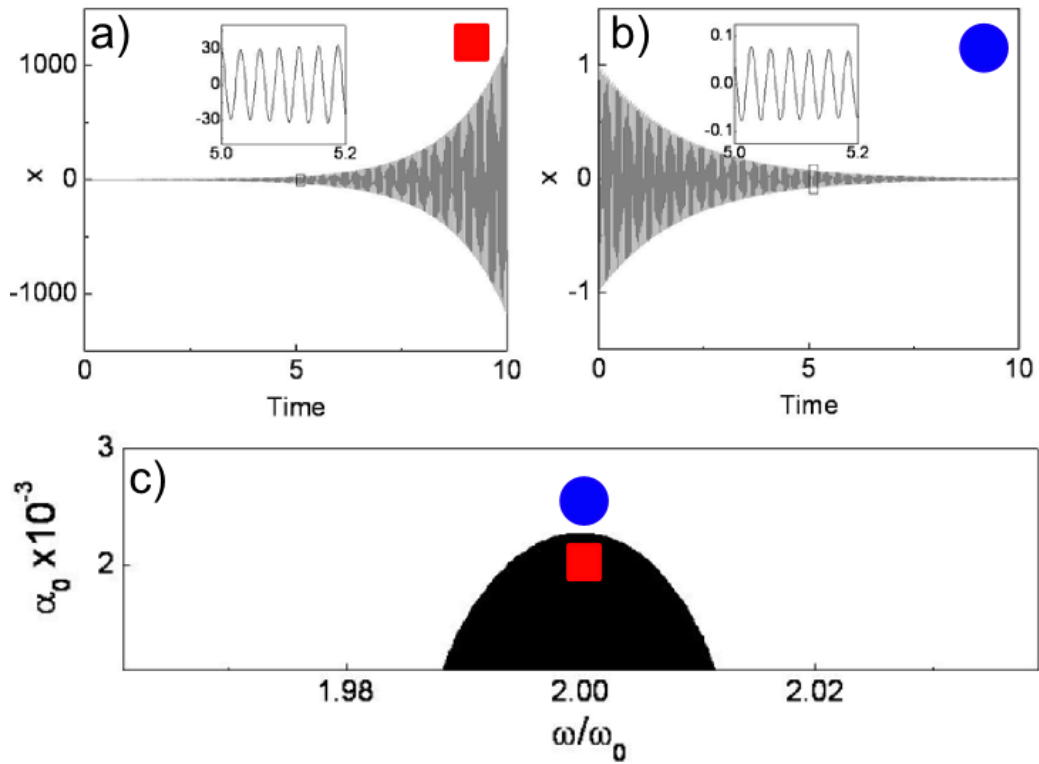


Figure 2.7: a and b show amplitude vs. time for parametric resonance in and outside of the instability zone. c shows a phase diagram of the parameters. The x-axis depicts the frequency, which excites the system and the y-axis the damping of the system. The black area represents a so called Arnold tongue, which is the area in parameter space, where parametric resonance is excited.

is shown in figure 2.6, where the x-axis represents time and the y-axis the amplitude of the excitation.

However parametric resonance (timevarying damping) is different, because it exhibits an instability phenomenon. Figure 2.7c shows a plot of the parameter space of parametric excitation. The y-axis represents the damping

and the x-axis the ratio between excitation frequency and eigen frequency. The black area, also known as Arnold tongue, denotes the region of instability, where parametric resonance is excited. The amplitude vs. the time in this region is shown in figure 2.7a. Figure 2.7b shows that outside of the black region, no resonance can be excited. The simulations show that parametric resonance is excited at about double the eigen frequency of the system.

Chapter 3

Experiment

3.1 Point Contact Technique

To experimentally observe the effect of STT, high electric current densities are required. This can be done by constricting the current flow to a small area with mechanic [24, 26, 31, 32, 33, 34, 35, 36, 37] or lithographic [38, 39, 40, 41, 42, 43] point contacts, or pillar devices [11, 44, 45, 46]. In our experiments we produce sharp tips by electrochemical etching to make mechanical point contacts to the samples.

The disadvantage of point contacts compared to other techniques is, that they are very sensitive to temperature variations, and small vibrations and movements. But they are also easy to make and less expensive than other approaches. Furthermore, smaller contacts than with electron beam lithography are possible.

The first step of making a point contact is to prepare a Cu tip by electrochemical etching. For that, a short piece of Cu wire ($\varnothing 250\mu\text{m}$) is connected to the positive electrode of a voltage source, which can apply up to 18.5V . The negative electrode, made of stainless steel, is placed in a solution of 45% KOH. By bringing the Cu wire into the KOH solution, it starts to react with the KOH, that means Cu^+ ions separate and react with the KOH, which is split into K^+ and OH^- . During that process a current between $0.5 - 0.8\text{mA}$ is flowing and depending on the conditions of the etching, a sharp tip is created. The tip is checked under a microscope and afterwards cleaned in DI water and Acetone.

Once the sharp tip is created, a critical point is to bring the tip in contact with the sample. This has to be done very carefully, since it is likely to destroy the nanostructure, by crashing the tip into the sample. To move the tip towards the sample, a standard differential screw mechanism is used. The functional principle of this mechanism is explained in reference [47]. One advantage of this technique is precision, since the tip is only moved by about $25\mu\text{m}$ for one turn of the control knob. Other advantages are the low costs and simplicity of the technique. The size of the point contact can be estimated by assuming a combination of ballistic and diffusive scattering as described in reference [48]. The area of point contacts is therefore in the size of a few hundred nm^2 . This results in high current densities up to $10^{13}\text{A}/\text{m}^2$.

Sample	Switching Current (A/m ²)	Switching time (P→AP)	Switching time (AP→P)
PMA	3.8×10^{11}	0.05 ns	0.028 ns
canted	2.5×10^{11}	0.045 ns	0.026 ns
In-plane	2.7×10^{12}	0.139 ns	0.169 ns

Table 3.1: Switching current and switching time for different magnetization anisotropies obtained by micromagnetic simulations.

3.2 Spin Transfer Torque Driven Magnetic Switching

In the scope of this section, the efficiency of STT in magnetic switching processes of samples with different tilt is going to be compared. There are different attempts to reduce switching currents of SVs or MTJ devices. One is to introduce tilted or perpendicular magnetizations, which also can improve the scalability in memory devices. As part of the work, micromagnetic simulations were done by F. Ferdousi and U. Roy supervised by Dr. S. Banerjee. Here only the results are given and details about the simulations can be found in [49]. The focus will be on the experimental part: First the preparation of the samples with different tilt of the layers are discussed, then the characterization and finally the point contact measurements to evaluate the efficiency of STT effects.

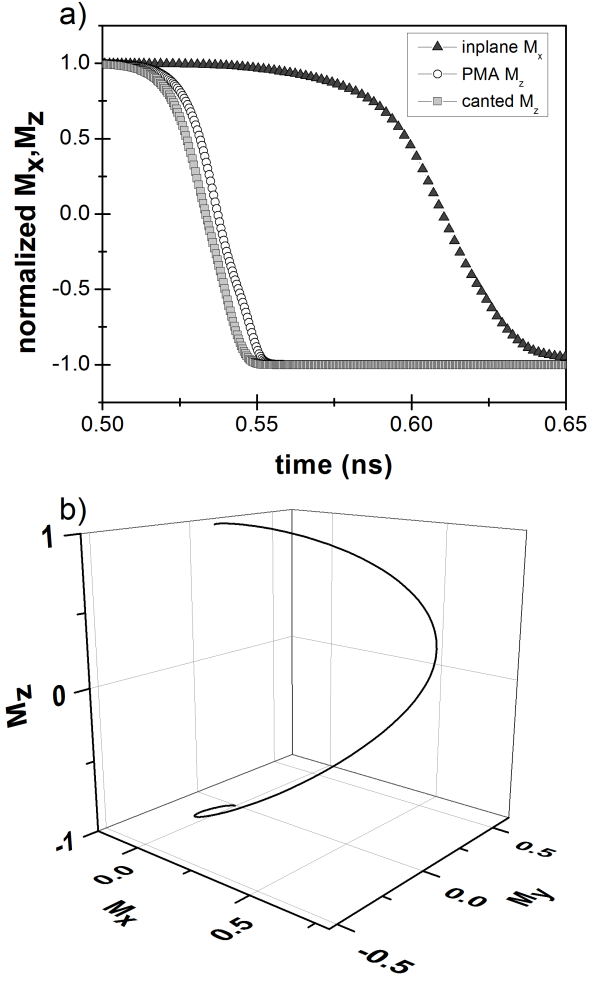


Figure 3.1: Simulation of magnetization dynamics at a current density of 4×10^{12} A/m² a) M_x (M_z) component of the free layer magnetization for in-plane (PMA and canted) SV: The switching time is improved for canted and perpendicular (PMA) magnetic anisotropy compared to the in-plane layer. b) Trajectory of the free layer magnetization during switching from parallel (P) to anti-parallel (AP) state for the canted spin valve.

3.2.1 Micromagnetic Simulations

The magnetic dynamics of the free layer were simulated using OOMMF [50]. There were no thermal or exchange bias effects taken into account and the field-like torque was assumed to be 30% of the STT. The cross sectional area of the spin valve in the simulations was elliptical, with short and long axes 40nm and 90nm, respectively. To compare the simulations with the experiment, three different free layer configurations were simulated: One with perpendicular magnetic anisotropy (PMA), one with a 45° tilt out of the plane, and one in-plane magnetization. The saturation magnetization for the PMA and canted layer was assumed to be 4×10^5 A/m and for the in-plane layer 1.45×10^6 A/m. For the PMA and canted layers, the anisotropy energies were taken as 1.1×10^5 J/m³ and 1.1×10^6 J/m³, while for the in-plane layers 1.2×10^5 J/m³ and 5.2×10^5 J/m³ was chosen. To estimate the switching current and investigate the switching properties of the different layers, 2 ns current pulses with current densities of 4×10^{12} A/m² and both polarities were simulated.

Figure 3.1 shows the switching dynamics for the three different simulated layers. The switching of the in-plane layer takes much longer than the layer with perpendicular or canted magnetization. The same trend can be seen in table 3.1, which shows that the in-plane layer needs much higher switching currents than the layers with canted or perpendicular magnetization.

3.2.2 Sample Preparation and Characterization

To compare the efficiency of STT in samples with different tilt of magnetization, samples with perpendicular, tilted, and in-plane magnetization were prepared. All samples in this chapter were made by F. Ferdousi and U. Roy supervised by Dr. S. Banerjee from the Microelectronics Research Center (MRC) at The University of Texas at Austin.

Both reference and free layer of the in-plane sample (sample V) were chosen to be Co and for the tilted and PMA samples (samples I to IV) Co/Pt and Co/Ni layers were deposited. The advantage of using Co/Pt and Co/Ni of different thickness and repetition is, that the tilt of the magnetization of the sample can be varied. This makes it possible to produce samples with different tilt, which can be compared.

The substrate of all samples were chosen to be p-Si(100) wafer. First they were piranha cleaned and wet-oxidized to grow a about 400nm thick silicon-dioxide (SiO_2) layer on which the seed layer of TaN/Ta/Pd was deposited. The seed layer is important to grow a (111) orientated crystalline stack. The thicknesses of these layers were selected to yield small root mean square (RMS) roughnesses. While the TaN and Ta layers were DC magnetron sputter deposited the Pd layer was electron beam evaporated. The Co, Pt, Ni and Co of reference and free layer were electron-beam evaporated with a deposition rate less than 0.1 Å/s and a pressure less than 5×10^{-6} Torr. All samples have a seed layer of TaN(400)/Ta(50)/Pd(150) and the thicknesses are given in Å. The compositions of sample I to IV are respectively:

- $Co(4)/[Pt(12)/Co(4)]_4/Cu(40)/Co(3)/Pt(10)/Co(3)/Pt(10)/cap$
- $Co(7)/Pt(16)/[Co(7)/Pt(17)]_3/Co(7)/Ni(7)/Co(4)/Cu(40)/Co(4)/Ni(6)/Co(2)/Pt(6)/cap$
- $[Co(4)/Pt(12)]_4/Co(2)/Ni(4)/Co(2)/Cu(40)/Co(2)/Ni(4)/Co(2)/Pt(6)/cap$
- $[Co(4)/Pt(12)]_4/Co(4)/Cu(40)/Co(15)/cap$
- $Co(50)/Cu(40)/Co(20)/cap$

Sample I to IV have a perpendicular top layer, while the magnetization of the reference layer is perpendicular or canted. Sample V is an in-plane sample.

The samples were characterized by XPS, AFM, XRD, VSM, EHE and MR measurements. In the following paragraphs first a short introduction to every method is given and then the results of the measurements are discussed briefly. XPS, AFM, and XRD measurements were done by F. Ferdousi and U. Roy supervised by Dr. S. Banerjee, and VSM measurements were done at the University of Minnesota.

X-ray Photoelectron Spectroscopy (XPS)

X-ray photoelectron spectroscopy is a technique to investigate the elemental composition of a sample and the associated electronic state and binding

Sample	RMS roughness (nm)	MR (%)	tilt of reference layer	point contact resistance (Ω)	point contact radius (nm)	slope upsweep (T/A)	slope downsweep (T/A)
I	0.978	0.11	-	11.0	15.8	no STT effect	no STT effect
II	1.270	0.34	45°	15.1	13.2	13.7	-10.9
III	0.860	0.19	12°	12.0	15.0	1.82	-6.75
IV	0.685	0.07	0°	12.7	14.6	-	-
V	-	0.21	in-plane sample	11.8	15.2	-0.281	-0.441

Table 3.2: Characteristic values for sample I to IV discussed in section 3.2.

Element	Binding Energy (eV)	Atomic Percentage(%)	FWHM
	778.19	27.41	1.345
Co 2p	793.84	25.49	3.4506
	780.56	47.09	5.5173
	852.43	37.59	1.23
Ni 2p	869.85	24.92	2.6
	855.47	37.48	6.49
Cu 2p	932.51	69.28	1.18
	952.33	30.72	1.64
Pd 3d	335.18	47.06	1.21
	340.5	42.94	1.38
Pt 4f	71.3	51.78	1.23
	74.62	48.22	1.47

Table 3.3: XPS measurement for sample II [49]

energy. This technique is sensitive to the surface of the sample. To get a depth profile the sample was etched and then scanned. The characterization was done for sample II and the outcome is summarized in table 3.3. While Pt and Pd do not show any oxidation peaks, the Cu barrier is oxidized, which does not seem to decrease the quality of the magnetic properties of the sample. [49]

Atomic Force Microscopy (AFM)

To examine the surface structure and the associated RMS roughness atomic force microscopy (AFM) in tapping mode is used. As was also shown in [51] the RMS roughness is improved by the Pd-layer. The RMS roughness values are summarized in table 3.2.

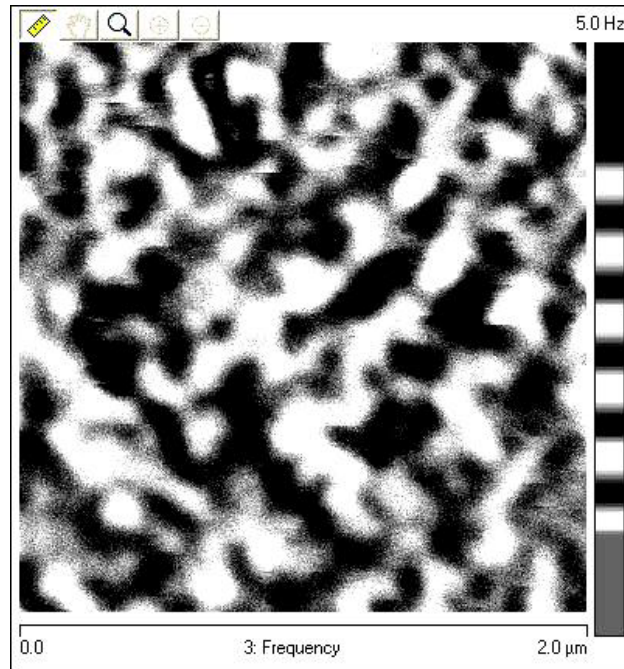


Figure 3.2: MFM scan of the demagnetized sample II. The scan area is $2\mu\text{m}\times 2\mu\text{m}$ and the black and white areas stand for domains with spin up and down. [49]

Magnetic Force Microscopy (MFM)

The domain structure of the demagnetized sample II is shown in figure 3.2. The single magnetic domains can be seen as black and white areas. The technique of tapping mode scanning in lift mode in a Dimension V microscope is described in reference [49].

X-ray diffraction (XRD)

To investigate the atomic structure of the samples, X-ray diffraction (XRD) was performed. The results for sample II are shown in figure 3.3.

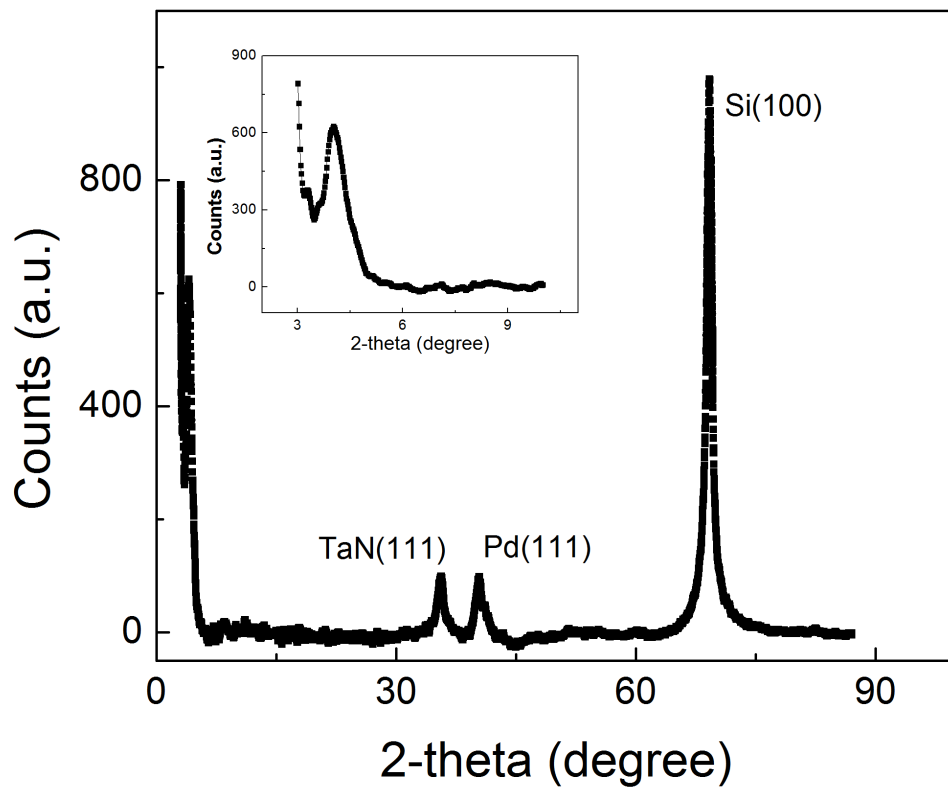


Figure 3.3: XRD analysis for sample II: Because of the very thin layers, only the peaks due to the thicker seed layers show up.

The main peak is at 69° and can be attributed to Si(100) [49]. The peak at 35.6° is due to TaN(100) and the peak at about 40° is mostly coming from Pd(111) and Pt(111) [49]. There is no evidence for Co(111), Cu(111) and Ni(111), which are at 44.2, 43 and 44.5 respectively [49]. This is probably because these layers are very thin compared to the others, and close to Pd/Pt(111). XRD measurements for the other samples look very similar, since the seed layers are the same.

Vibrating Sample Magnetometer (VSM)

Vibrating sample magnetometer (VSM) measurements were performed at the University at Minnesota to determine the canting of the reference layer. According to reference [51] the tilting of a magnetic layer can be obtained by carrying out VSM measurements in- and out-of-plane of the samples. The tilting can then be calculated by the ratio of remanence and saturation magnetization. This was done for only the reference layer and also the whole stack. For sample II for instance the tilting without free layer was obtained to be about 40° and for the whole stack about 45° . Since the free layer is almost the same and very thin, it can be said that the main difference is coming from the reference layer and in table 3.2 the tilting obtained for the whole samples are given. Though this technique, to obtain tilting, is only valid in the framework of Stoner-Wohlfarth particles, it can also be applied to our samples, since they consist of coupled grains, with a grain size much smaller than the size of a single domain[51]. More details of the VSM

measurements can be found in reference [49].

Extra-Ordinary Hall Effect (EHE) and Magneto Resistance (MR)

Extra-Ordinary or anomalous Hall Effect (EHE) is an additional term in the normal Hall resistivity of ferromagnets, when the field is applied perpendicular to the sample plane. The deviation from the normal Hall effect is due to skew scattering and side-jump mechanisms[8, 52].

EHE and magneto resistance (MR) measurements for samples I to VI are shown in figure 3.4. For sample I the hysteresis loop of the EHE measurement is squared and a distinct switching of the two layers is visible. For samples II to IV, the separate switching of free and reference layer cannot be observed. However for samples III and IV the hysteresis loop is mostly squared, which is due to the strong PMA of Co(4)/Pt(12) multilayers. Nevertheless all four samples show separate switching of reference and free layer in the MR measurements. The MR values of all samples are summarized in table 3.2.

3.2.3 Point Contact Experiments

For all samples point contact measurements were performed, to draw conclusions about the efficiency of STT depending on the tilting of the reference layer. In Fig 3.5a one typical MR measurement in point contact geometry, with a fixed dc current, of sample II is shown. Starting from a high negative applied magnetic field, both layers are parallel and the resistance is in low

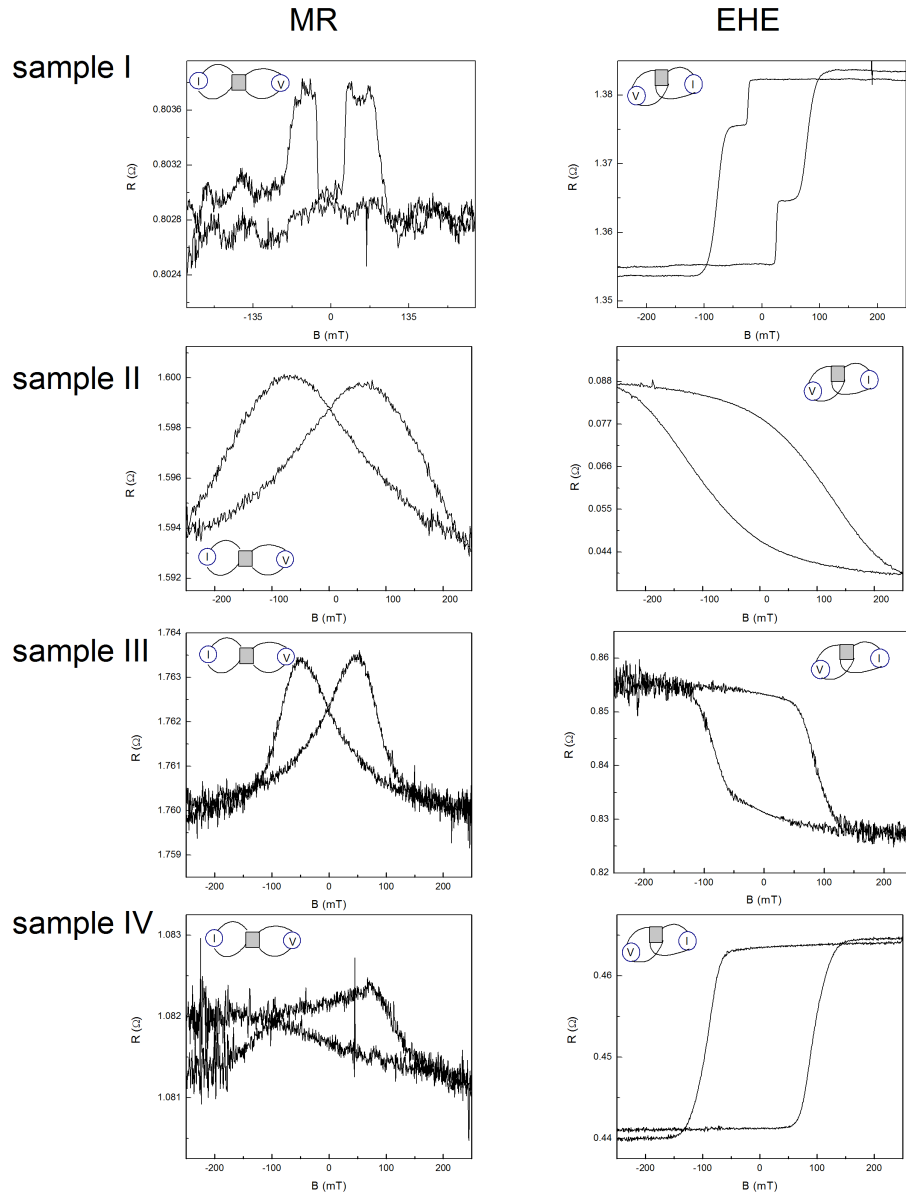


Figure 3.4: MR and EHE measurements for sample I to IV: All four samples show separate reference and free layer switching in the MR measurements, while in the EHE measurements, this can only be observed for sample I.

state. If we increase the field to positive values (upsweep), the free layer switches at a small positive field, while the reference layer stays the same. This can be seen as a resistance jump in the MR trace, since the resistance depends on the alignment of the two layers. By increasing the field even more, also the reference layer switches and the sample goes back into the low resistance state. The same is happening when the magnetic field is ramped from high positive to high negative fields (downsweep). Similar traces were observed for the other samples.

To evaluate the efficiency of STT in samples I to III and V, this MR trace is recorded for different applied dc currents. Then the current is plotted vs. the switching field and fitted linearly. A higher slope in these plots indicates, that less spin current is needed to change the switching field and therefore STT is more efficient.

Sample I does not show any dependence of the switching field on the applied field, probably due to spin-scattering effects of the Pt layers close to the non-magnetic Cu spacer. The slopes for perpendicular applied field for sample II and III, and parallel applied field for sample V are listed in table 3.2 and the corresponding plots are shown in figure 3.5. Both in micromagnetic simulations of section 3.2.1 and in point contact experiments, the efficiency of STT for the in-plane sample (sample V) is the lowest, while for the sample with 45° tilt (sample II) it is very high. This improvement of STT efficiency in sample II is probably due to the tilted polarization of the reference layer,

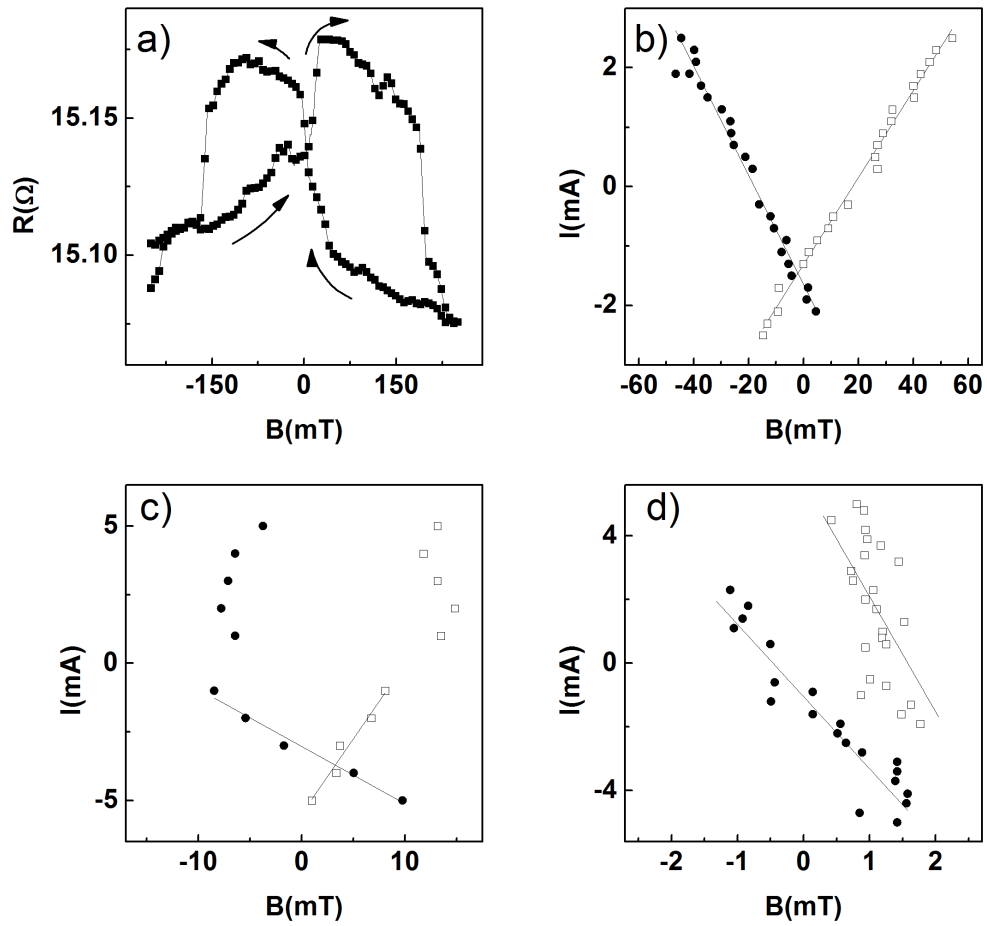


Figure 3.5: a) typical MR trace in point contact geometry for sample II
b-d) Current vs. switching field for sample II, III and IV

which can introduce precessional switching.

The slopes of sample II and III can be explained as followed: With increasing negative current during upsweep, more and more electrons are injected to the sample through the free layer. This helps the magnetic field to switch the free layer into an antiparallel state with respect to the reference layer. Therefore the field needed to switch the free layer decreases. However with increasing positive current, more and more electrons are flowing through the reference layer to the free layer, and the resulting torque helps to keep the free layer parallel to the reference layer. This makes free layer switching more difficult and higher fields have to be applied to switch the free layer in parallel state. The same arguments hold for the downsweep.

Sample III shows a different slope for positive current, that means electrons flowing from the reference layer to the free layer. When the sign of the current is reversed from negative to positive, the spin current tries to keep the free layer parallel, but if the applied field is directed in such a way, that it helps to switch the free layer, the magnetic domains of the free layer can get canted away from the perpendicular direction, which could result in a change of slope [52]. Another reason for this effect could be, that the tilted reference layer introduces a non-uniform effective field on the free layer[53]. Similar effects, could be the reason that the slope for upsweep of sample V is negative.

Table 3.2 also lists the point contact resistances and corresponding point contact radii. The size variation between these contacts is about 20%, while the

observed variations in STT slope is much larger than this variation. Thus it can be concluded, that for a qualitative comparison, it is justified to compare the slopes with respect to the current and not the current density.

For sample IV and V, angular dependent measurements were performed and in figure 3.6 grey scale plots for sample IV are shown. The x-axis depicts the magnetic field, while the y-axis represents the applied dc current. Different grey shades indicate different resistances, that means the lighter the grey, the higher the resistance measured in the experiment. And the angles indicate the angle of the applied field with respect to the plane of the sample. For 90° , that means a perpendicular applied field, the resistance changes slowly with varying magnetic field and no distinct switching, like in figure 3.5a, can be observed. However for 0° and 45° distinct switching of different layers can be seen. The resistance changes for 0° are distributed and no STT effect can be observed. At this angle the in-plane layer of sample IV is at 0° , but the perpendicular layer is probably canted out of the plane of the sample. This might be the reason, that the switching is distributed and the final angle of the reference layer varies among the measurements. Nevertheless the grey scale plot for 45° shows distinct switching events and STT effect. The change in resistance at about ± 10 mT shows no STT effect, however the change in resistance at about ± 30 mT to ± 60 mT, certainly does. The switching field clearly changes with applied dc current. Both, up sweep and downsweep, have a negative slope, which is probably due to similar effects

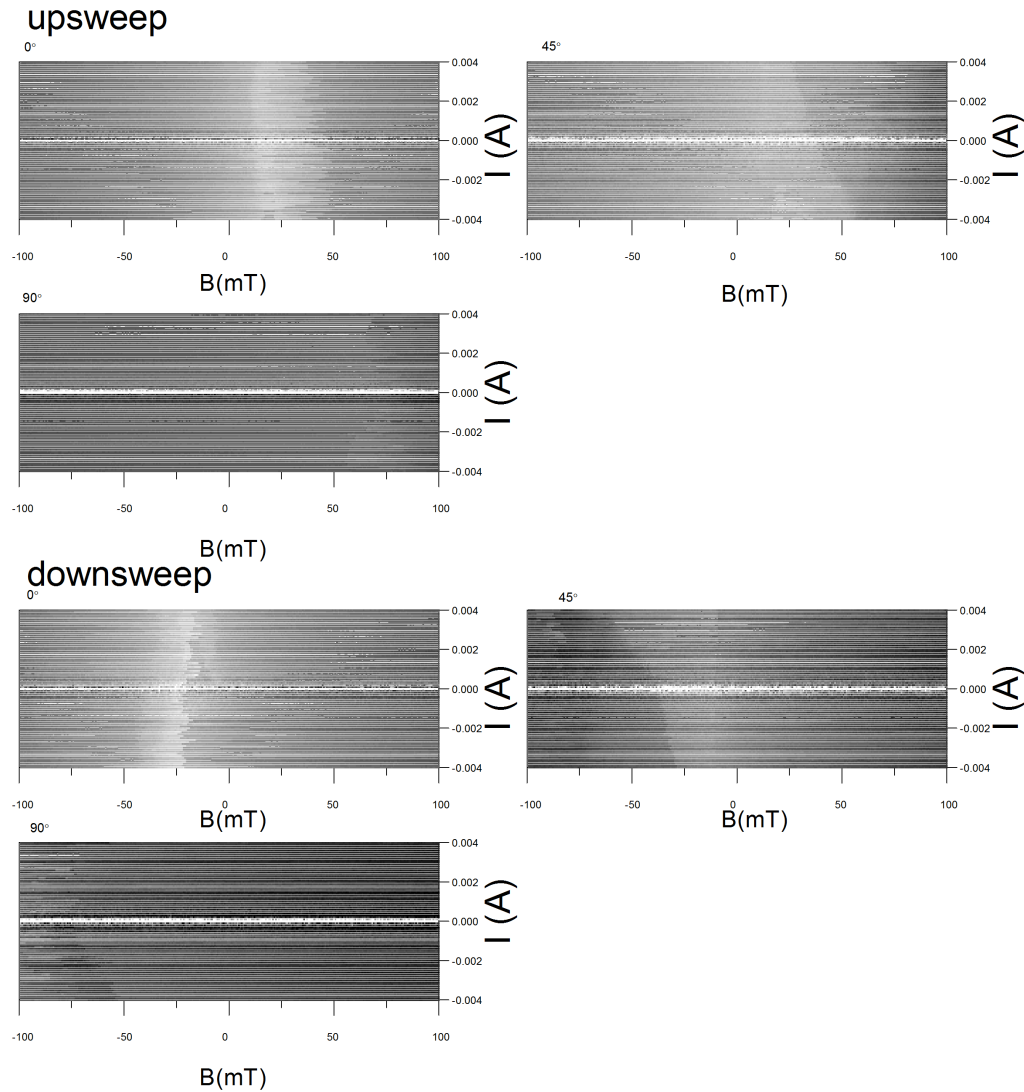


Figure 3.6: Grey scale plots for sample IV for up- and downsweep: The x-axis represents the applied magnetic field, the y-axis the applied dc current and different grey shades indicate different resistances (dark - low resistance; light - high resistance). The magnetic field was applied at different angles (0° , 45° and 90°) in respect to the plane of the sample. For 90° no distinct switching of the two layers can be observed. However for 0° and 45° distinct switching events are visible and for 45° STT effect can be observed.

as explained for sample V.

Figure 3.7 shows a different grey scale plot for sample V. Here the x-axis still depicts the magnetic field, while the y-axis shows the angle of the magnetic field. The magnetic field is applied parallel to the sample plane, so the angles are with respect to the initial position of the sample in the experiment. Upsweep and downsweep look similar, but there is a change of switching fields with varying angle. The grey scale plot repeats every 180° , which is expected, since the switching depends on the angle of the magnetic field in respect to the easy axis of the sample. The easy axis is to be expected at about $80^\circ/260^\circ$, where the switching can be described as a simple up- and downstep. For some angles (about 0° to 50° and 160° to 230°) the switching is not a simple MR curve, and two different high resistance regions, can be observed. It could be that the applied magnetic field, is not perfectly aligned to the sample plane, and magnetic moments get canted out of the plane, or other effects, maybe due to the deposition conditions, evoke those switching events.

3.2.4 Discussion

In this section five different multilayer stacks with different amount of tilt of the magnetization were compared. First some measurements to characterize the samples were performed (XPS, AFM, MFM, XRD, EHE and MR) and the tilt of the canted magnetizations was estimated via VSM measure-

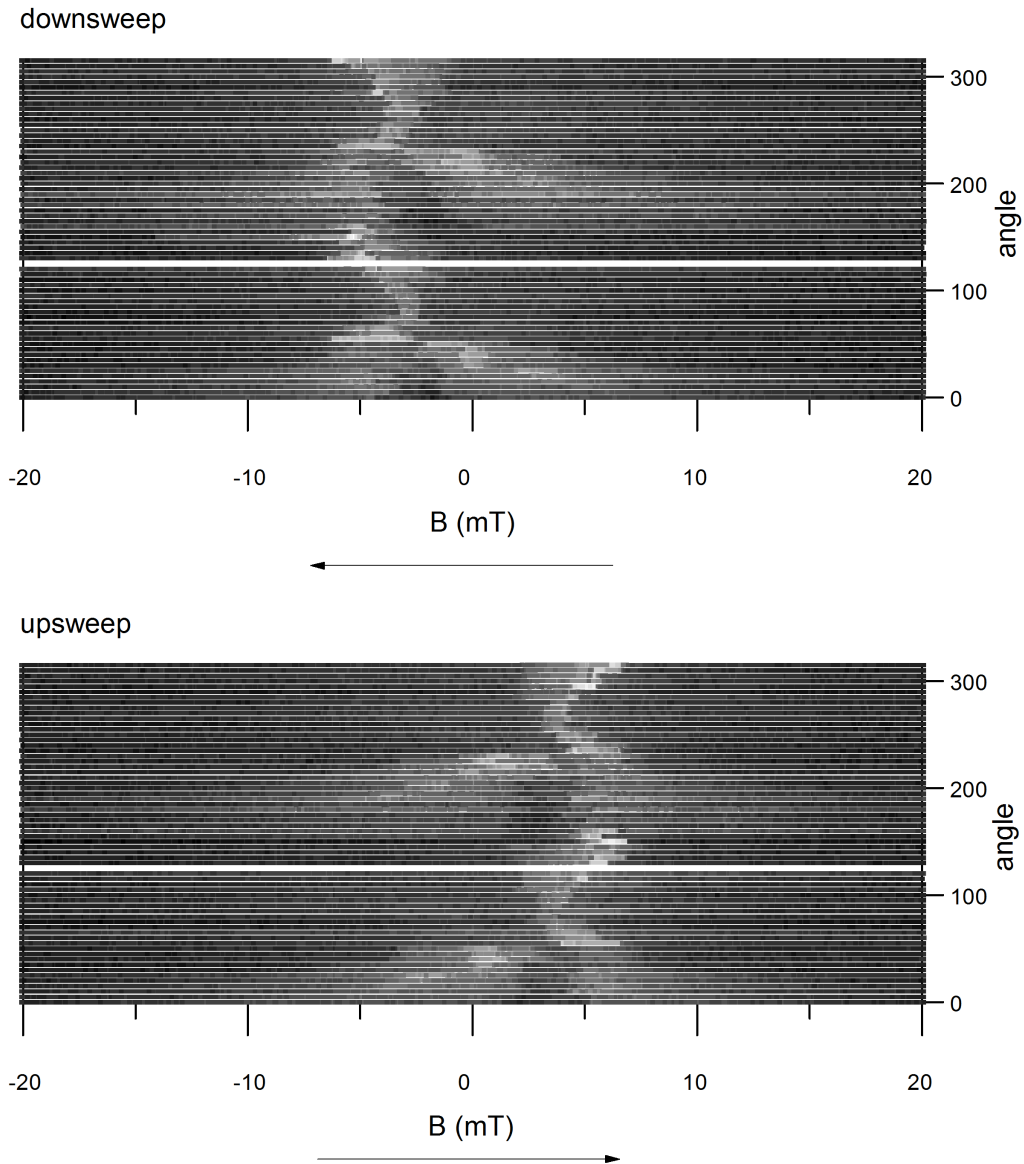


Figure 3.7: 3D plots of the angle dependence of sample V: The x-axis represents the applied field, the y-axis the angle of the applied in-plane field in respect to an arbitrary initial angle and different grey shades indicate different resistances (dark - low resistance; light - high resistance).

ments. Point contact measurements were done to compare the efficiency of STT in samples with different tilt. As expected STT is more efficient in the sample with a 45° tilt of the reference layer than in the sample with 12° tilt. Sample I showed no STT effects, probably due to the Pt layer close to the Cu layer and the in-plane sample showed very small STT effects. This was supported by micromagnetic simulations, which showed, that the switching current is smaller and switching is faster for magnetic layers with canted tilt. One reason for better switching conditions in samples with canted magnetic layers, might be that precessional switching takes place, as seen in the switching event shown in the simulation in figure 3.1b. For sample IV and V angular dependent measurements were performed, showing that the switching and STT effects can depend strongly on the angle. Sample IV showed STT effects for a magnetic field applied at a 45° angle with respect to the sample surface, which is probably caused by tilting of the magnetic moments away from the applied field at about 0° or 90° .

Though it was shown, in experiment and micromagnetic simulation, that STT efficiency can be improved by tilting the magnetization of the reference layer, this is only a qualitatively comparison. Further experiments have to be done, for example with nanopillar devices.

3.3 Spin Transfer Torque Driven Magnetodynamics

3.3.1 Set-up and Sample

In the following the experimental set-up to examine STT driven FMR and the fabrication process of the sample are discussed.

The sample used in the experiments is an exchange-biased spin valve (EBSV) with two FM layers (NiFe) separated by a non-magnetic spacer (Cu). The composition is given by IrMn(10 nm)/NiFe(10 nm)/Cu(5 nm)/NiFe(4 nm), where the numbers in brackets are thicknesses of the layers. The layers were deposited by rf/dc magnetron sputtering in an ultrahigh-vacuum compatible system (base pressure 2×10^{-9} Torr). The substrate is oxidized Si and the sputtering was done in 5 mTorr of Ar. To protect the sample, it has a 1nm thick Cu cap and to ensure good CPP current flow, in the point-contact experiments, a 30 nm thick Cu underlayer. After all layers were deposited, the sample was heated to $\sim 600K$ and cooled down to room temperature in an external magnetic field of about 300 mT to induce exchange biased coupling at the interface of IrMn and NiFe.

The set-up to measure FMR excited by STT is shown in figure 3.8. The sample is placed in a pair of magnetic coils, so that the magnetic field is parallel to the sample plane. To measure the effects of dc and ac current,

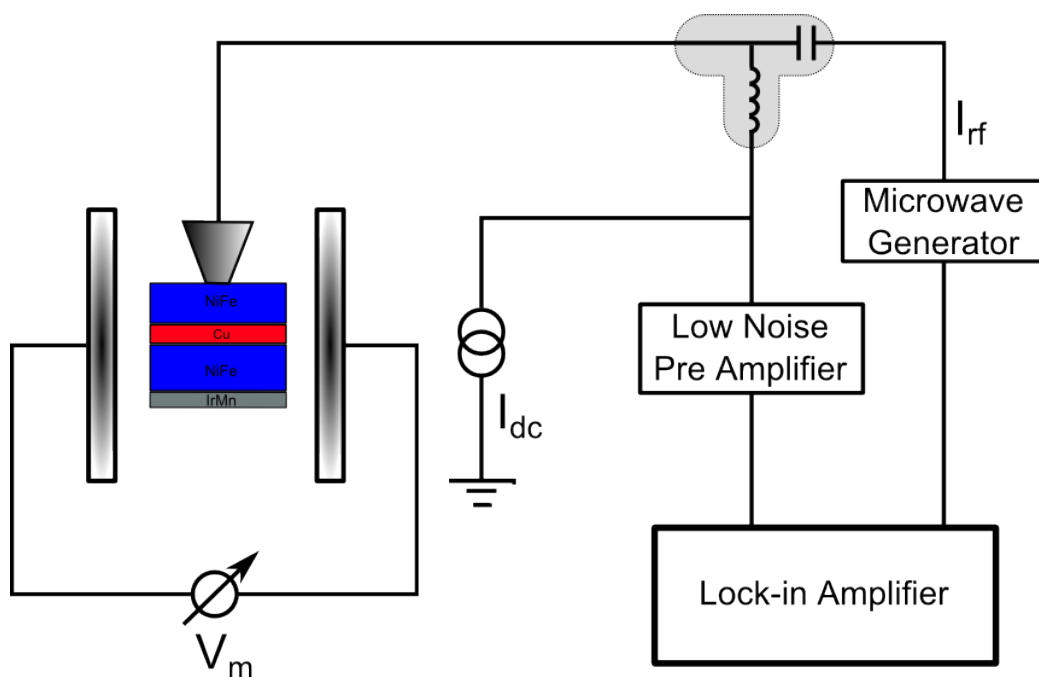


Figure 3.8: Schematic of the experimental set-up: A rf current, generated by a microwave generator, and a dc current are combined via a bias T and then injected through a point contact to the sample. An external magnetic field is applied by a pair of electric coils.

both current types can be applied via a bias T. The rf current is generated by a microwave generator and to reduce the noise of the signal a lock-in amplifier is used. As discussed in section 3.1 the current is injected through a mechanical point contact to the sample, while all the measurements are done at room temperature. The values which are measured in the experiment are the dc and rf current, the applied voltage to the magnetic coils, and rectified voltage. The data was taken with LabView and afterwards analysed with OriginLab.

3.3.2 Experiment - Ferromagnetic Resonance

First the sample was characterized by measuring STT driven FMR. The field dependence of the rectification voltage for an ac current of 21 GHz and no bias current is shown in figure 3.9a. The resistance of the point contact was 4.2Ω . The two dips in the voltage trace can be associated with FMR in a thin film. The effect of a dc current on the linewidth of the signal is shown in figure 3.9b. The width decreases linearly with increasing dc current, while the position and the amplitude are not affected. This linear dependence confirms that we observe FMR in a small volume of the contact, because only in this region the density of the current is high enough, and the STT results in a linear dependence of the damping and therefore the linewidth of the resonance structure. The solid and open circles refer to the resonance dip at negative and positive field, respectively. The asymmetry arises because neither the sample nor the set-up (Cu tip and sample) is symmetric. For high

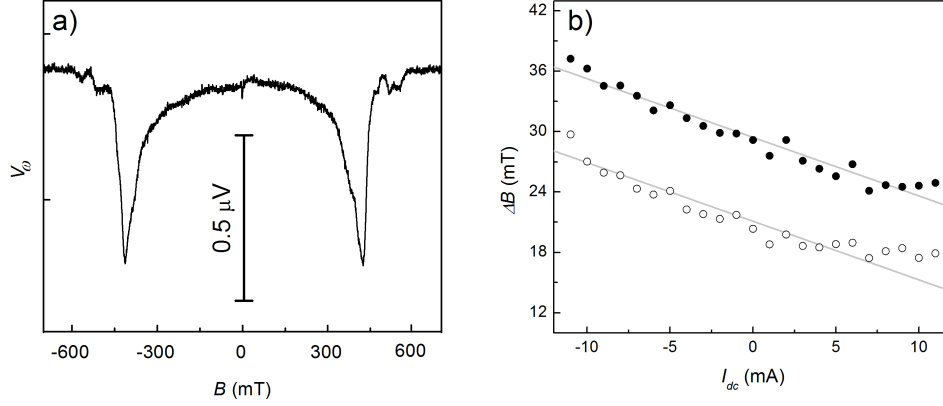


Figure 3.9: a) STT driven FMR at room temperature for a dc current of 21 GHz and no bias current applied to a 4.2Ω point contact b) linear dependence of the linewidth of the resonance signal on the applied dc current. Solid (open) circles refer to negative (positive) field.

positive and negative currents deviations start to increase, probably due to Joule heating.

The resonance dips at about ± 400 mT in figure 3.9a correspond to FMR of NiFe. In figure 3.10 the field dependence of the rectification signal is shown. For increasing frequency the resonance structure shifts to a higher applied magnetic field. If we plot frequency vs. field as in figure 3.10b, the data points can be well fitted with equation 2.26. Here γ is 28 GHz/T and $\mu_0 M$ is 0.9T as expected for bulk NiFe. This confirms that the observed resonance structure is due to FMR.

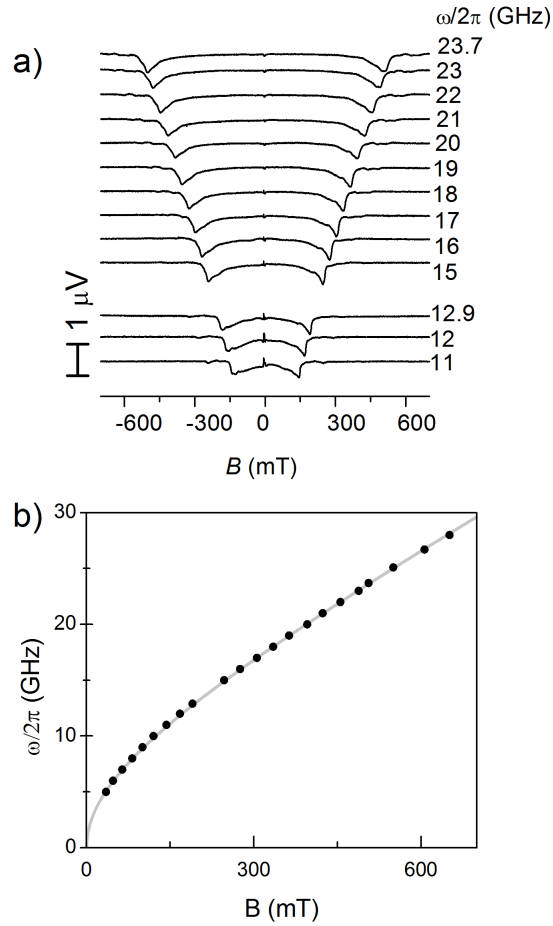


Figure 3.10: a) Field dependence of the rectification signal measured at different frequencies of the applied dc current: with increasing frequency the resonance dips shifts to higher magnetic fields. b) Field dependence of STT driven FMR: closed circles show the measured dependence from a) and the solid line the expected FMR relationship for bulk NiFe.

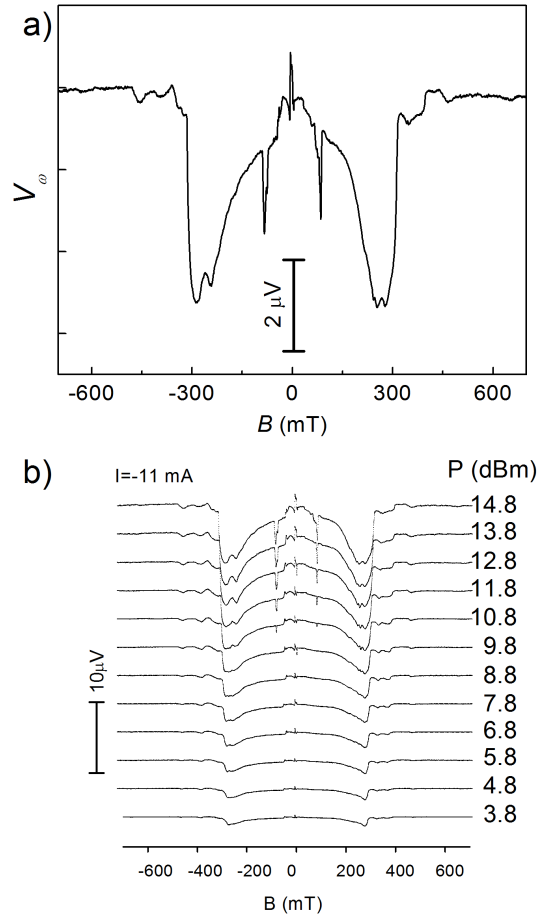


Figure 3.11: a) Resonance structure for an applied dc current of 21GHz, a power of 12.3 dBm and a dc current of -11mA: The dip at about ± 280 mT corresponds to FMR, while the dip at about ± 90 mT can be assigned to parametric resonance. b) Trace of the rectified voltage for increasing power up to 14.8dBm: Starting at about 10.8 dBm the second resonance dip due to parametric resonance appears.

3.3.3 Experiment - Parametric Resonance

In the previous section the sample was characterized by STT driven FMR, now we are going to focus on parametric resonance.

In figure 3.11a, a trace of the resonance signal for an applied ac current of 21 GHz with a power of 12.3 dBm, and a dc current of -11 mA is shown. The resonance structure at about ± 280 mT is due to FMR as discussed in section 3.3.2. However a second resonance dip at about ± 90 mT is showing up, which is due to parametric resonance. Figure 3.11b shows the trace of the resonance signal for different applied power values of the ac current. As expected for parametric resonance, a threshold power has to be applied to observe the additional dip. The position of the parametric resonance does not change noticeable with increasing power, however the amplitude increases.

The power dependence of FMR and parametric resonance is shown in figure 3.12a. The open symbols represent FMR and the closed symbols parametric resonance. It is clearly visible, that FMR has no threshold power and behaves differently (parabolic dependence) with increasing power. The parametric resonance however, does not show up before about 10 dBm. The measurements were done at an applied dc current of -11mA and an ac frequency of 16 GHz.

In section 2.4 it was discussed that parametric resonance is excited at double the FMR frequency. This is shown in figure 3.12b. Here the field dependence of STT driven FMR is shown like in figure 3.10b, however additionally the frequency dependence of parametric resonance is plotted. It can be fitted

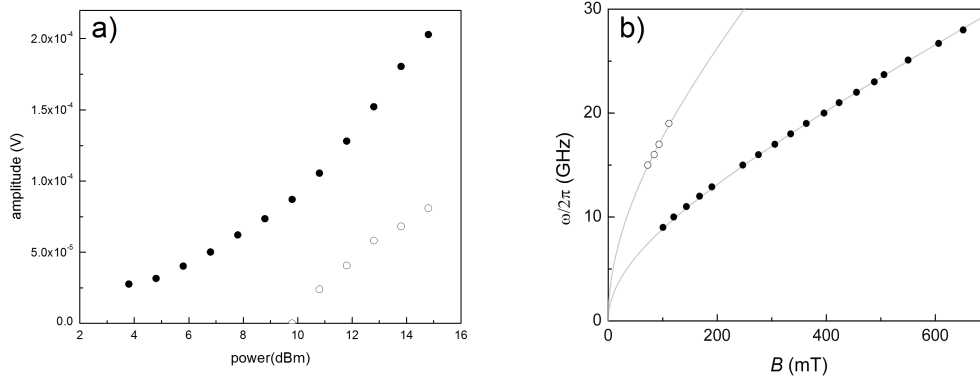


Figure 3.12: a) amplitude of FMR (closed circles) and parametric resonance (open circles) vs. the applied power b) Frequency vs. the switching field for FMR (closed circles) and parametric resonance (open circles) both fitted with equation 2.26.

with equation 2.26, as done for FMR.

In the grey scale plots in figure 3.13 the y-axis represents the applied current and the x-axis the magnetic field. The shade of the grey is measure for the rectified voltage. The darker the grey, the deeper the dip in the trace of the rectified voltage. The individual plots are for different power values of the ac current applied to the contact. In equation 2.28 we saw that the effective damping is a function of the current, therefore the y-axis is proportional to the damping. The x-axis (magnetic field) is function of the frequency of the resonance. Consequently figure 3.13 can be compared to figure 2.7c. The good agreement of these two figures is another evidence that parametric resonance was excited in the experiment.

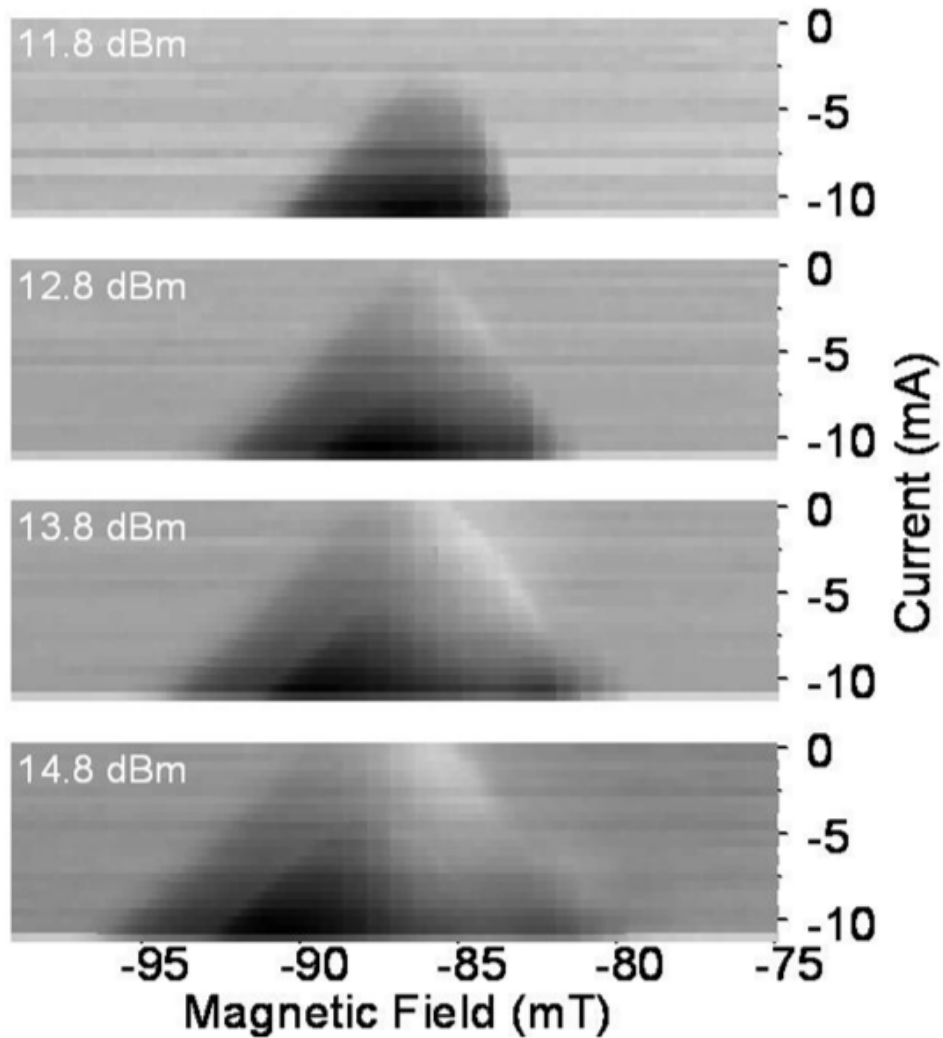


Figure 3.13: Grey scale plots of the parametric excitation for different applied power values of the ac current: The x-axis represents the magnetic field, the y-axis the applied current, and the shade of the grey displays the measured rectified voltage (the darker the grey, the deeper the dip of the resonance structure) The dark areas represent Arnold tongues, which are an evidence for parametric excitations.

3.3.4 Discussion

In this section an EBSV sample was first characterized by STT driven FMR in point contact geometry. The typical frequency dependence of the switching field and the linear dependence of the line width, therefore the damping, was observed. After these basic characterizations of the sample, the power was increased and after a threshold power was reached, a second resonance dip started to show up. This was shown to be due to parametric excitations. The parametric resonance in the experiment was driven by an ac current, which causes the damping to oscillate in time. Another proof that the observed resonance is actually due to parametric resonance was shown in grey scale plots, which clearly showed the existence of Arnold tongues. Remarkably, parametric resonance started to show up at about 10dBm applied power. Since only a few percent of this power actually reach the point contact, due to impedance mismatches, this is a relatively low power to excite parametric resonance. Parametric resonance is shown to increase approximately exponentially [30] under constant pumping and therefore the amplitude can grow faster than in conventional resonance. This could make parametric excitations interesting for applications like magnetic memory devices, since a faster growth of excitations can allow faster switching.

Chapter 4

Summary and Outlook

This thesis presented two experiments, exploring spin dynamics and the influence of STT. In both cases the currents were injected through a mechanical point contact and the sample was exposed to an external applied magnetic field.

In the first experiment SVs with different tilt of the reference layer and PMA in the free layer, were compared. As expected, we saw that STT is more efficient for SVs with tilted magnetization, compared to the SV with in-plane magnetic anisotropy. Also, the sample with 45° tilt, showed a higher dependence of the switching field on the current than the sample with 12° tilt. The experimental results were emphasized by micromagnetic simulations, imitating magnetic layers with different tilt. In the future similar experiments with different FM materials and/or different layerthicknesses could be performed to lower switching currents and switching times. Another approach could be,

to use tunnel oxides like MgO as NM spacers with FM dots to inject current. In the second part of this thesis, ac and dc currents were applied to an EBSV to perform resonance experiments. First the sample was characterized by STT driven FMR. After that, the applied power was increased and parametric resonance was observed. As expected, the resonance due to parametric excitations has a threshold power and typical Arnold tongues in 3D plots could be observed. In future experiments, EBSV with different materials or stacks could be investigated, to lower the threshold power and therefore lay the foundation to make parametric resonances applicable in high frequency electric devices.

Bibliography

- [1] D.C. Ralph and M.D. Stiles, *J. Magn. Magn. Mater.* **320**, 1190 (2008)
- [2] I. Žutić *et al.*, *Rev. Mod. Phys.* **76**, 323 (2004)
- [3] S.A. Wolf *et al.*, *IBM J. Res. & Dev.* **50**, 101 (2006)
- [4] S.A. Wolf *et al.*, *Science* **294**, 1488 (2001)
- [5] M.N. Baibich *et al.*, *Phys. Rev. Lett.* **61**, 2472 (1988)
- [6] G. Binasch *et al.*, *Phys. Rev. B* **39**, 4828 (1989)
- [7] N.F. Mott, *Adv. Phys.* **13**, 325 (1964)
- [8] J.M.D. Coey, *Magnetism and Magnetic Materials*, Cambridge University Press, New York (2009)
- [9] E. Y. Tsymbal and D. G. Pettifor, *Perspective of Magnetoresistance*, in: H. Ehrenreich and E. Spaepen (eds.) *Solid State Physics* **56**, page 113, Academic Press, New York (2001)
- [10] M. Tsoi *et al.*, *Phys. Rev. Lett.* **80**, 4281 (1998)

- [11] J.A. Katine *et al.*, Phys. Rev. Lett. **84**, 3149 (2000)
- [12] A.A. Tulapurkar *et al.*, Nature **438**, 339 (2005)
- [13] J.C. Sankey *et al.*, Phys. Rev. Lett. **96**, 227601 (2006)
- [14] G.S.D. Beach *et al.*, J. Magn. Magn. Mater. **320**, 1272 (2008)
- [15] C. Kittel, *Introduction to Solid State Physics*, John Wiley & Sons, Inc., eighth edition, (2005)
- [16] S. V. Vonsovskii, *Ferromagnetic Resonance: The Phenomenon of Resonant Absorption of a High-Frequency Magnetic Field in Ferromagnetic Substances*, Pergamon Press Ltd., Oxford, first english edition (1966)
- [17] C. P. Schleicher, *Principles of Magnetic Resonance*, Springer Verlag, Berlin Heidelberg New York, second revised and expanded edition (1978)
- [18] R. Skomski, *Simple Models of Magnetism*, Oxford University Press, Oxford (2008)
- [19] L. Landau and E. Lifshitz, Phys. Z. Sowjet. **8**, 153 (1935)
- [20] T.L. Gilbert, IEEE Trans. Magn. **40**, 3443 (2004)
- [21] O. Posth *et al.*, J. Phys. D: Appl. Phys. **42**, 035003 (2009)
- [22] W. Chen *et al.*, Appl. Phys. Lett. **92**, 012507 (2008)
- [23] Y. Huai *et al.*, Appl. Phys. Lett **84**, 3118 (2004)

- [24] J. C. Slonczewski, J. Magn. Magn. Mater. **159**, L1 (1996)
- [25] J.C. Slonczewski, J. Magn. Magn. Mater. **247**, 324 (2002)
- [26] M. Tsoi *et al.*, Nature **406**, 46 (2000)
- [27] N. Mecking *et al.*, Phys. Rev. B **76**, 224430 (2007)
- [28] W.B. Case, Am. J. Phys. **64**, 215 (1996)
- [29] P. L. Tea and H. Falk, Am. J. Phys. **36**, 1165 (1968)
- [30] S.M. Curry, Am. J. Phys. **44**, 924 (1976)
- [31] W.H. Rippard *et al.*, Appl. Phys. Lett. **82**, 1260 (2003)
- [32] Y. Ji *et al.*, Phys. Rev. Lett. **90**, 106601 (2003)
- [33] I.K. Yanson *et al.*, Phys. Rev. Lett. **95**, 186602 (2005)
- [34] O. P. Balkashin *et al.*, Phys. Rev. B **79**, 092419 (2009)
- [35] Z. Wei *et al.*, Phys. Rev. Lett. **98**, 116603 (2007)
- [36] Y. Luo *et al.*, New J. Phys. **9**, 329 (2007)
- [37] X.J. Wang *et al.*, Appl. Phys. Lett. **93**, 162501 (2008)
- [38] W.H. Rippard *et al.*, Phys. Rev. Lett. **92**, 027201 (2004)
- [39] S. Kaka *et al.*, Nature **437**, 389 (2005)
- [40] F.B. Mancoff *et al.*, Nature **437**, 393 (2005)

- [41] O. Ozatay *et al.*, Appl. Phys. Lett. **88**, 202502 (2006)
- [42] Q. Mistral *et al.*, Phys. Rev. Lett. **100**, 257201 (2008)
- [43] S. Bonetti *et al.*, Appl. Phys. Lett. **94**, 102507 (2009)
- [44] J. Grollier *et al.*, Appl. Phys. Lett. **78**, 3663 (2001)
- [45] M. Tsoi *et al.*, Phys. Rev. Lett. **93**, 036602 (2004)
- [46] S. Urazhdin *et al.*, Phys. Rev. Lett. **91**, 146803 (2003)
- [47] E. Y. Tsybal and I. Žutić, eds., *Handbook of Spin Transport and Magnetism*, Chapman and Hall/CRC (2012)
- [48] Z. Wei *Spin-Transfer-Torque Effect in Ferromagnets and Antiferromagnets*, PhD dissertation, University of Texas at Austin, Department of Physics (2008)
- [49] F. Ferdousi, *Device Design and Process Integration of High Density Non-volatile Memory Devices*, PhD dissertation, University of Texas at Austin, Department of Electrical and Computer Engineering (2011)
- [50] M. J. Donahue and D. G. Porter, OOMMF Users Guide, National Institute of Standards and Technology Report No. NISTIR 6376 (1999), unpublished.
- [51] C.L. Zha and J. Åckerman, IEEE Trans. Magn. **45**, 3491 (2009)
- [52] L. Berger, Phys. Rev. B **2**, 4559 (1970)

[53] O.J. Lee *et al.*, Appl. Phys. Lett. **95**, 012506 (2009)